CHEMICAL REVIEWS

pubs.acs.org/CR

Review

Design Principles of Colloidal Nanorod Heterostructures

Gryphon A. Drake, Logan P. Keating, and Moonsub Shim*

Cite This: https://doi.org/10.1021/acs.chemrev.2c00410

Read Online

ACCESS | Metrics & More | Article Recommendations

ABSTRACT: Anisotropic heterostructures of colloidal nanocrystals embed size-, shape-, and composition-dependent electronic structure within variable three-dimensional morphology, enabling intricate design of solution-processable materials with high performance and programmable functionality. The key to designing and synthesizing such complex materials lies in understanding the fundamental thermodynamic and kinetic factors that govern nanocrystal growth. In this review, nanorod heterostructures, the simplest of anisotropic nanocrystal heterostructures, are discussed with respect to their growth mechanisms. The effects of crystal structure, surface faceting/energies, lattice strain, ligand sterics, precursor reactivity, and reaction temperature on the growth of nanorod heterostructures through heteroepitaxy and cation exchange reactions are explored with currently known examples. Understanding the role of various thermodynamic and kinetic parameters enables the controlled synthesis of complex nanorod heterostructures that can exhibit unique tailored properties. Selected application prospects arising from such capabilities are then discussed.

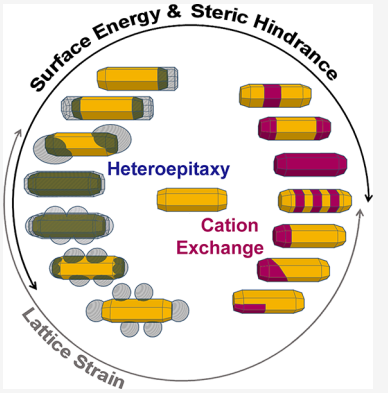

CONTENTS

1. INTRODUCTION

Colloidal quantum dots exhibit high performance of crystalline inorganic semiconductors while emulating versatility, precision, and processability of molecular materials. One of the key breakthroughs that has enabled their incorporation into consumer products has been the development of core/shell structures that have drastically improved their optical properties, stability, and therefore applicability.[1−7] Hence, heterostructures, defined here as two or more semiconductors brought together with well-defined epitaxial relations, are often essential for advancing applications incorporating colloidal quantum dots. Core/shell quantum dots, which may be

Special Issue: Anisotropic Nanomaterials

Received: June 14, 2022

considered as isotropic heterostructures, have been utilized in many applications including color converters in displays, light emitting diodes, photovoltaics, lasers, and biolabels.[8−16] Band-structure engineering through varying size and composition and solution processability have enabled the development of these applications.

Emerging anisotropic heterostructures can vastly expand the range of tailored properties and impart new capabilities through additional tunable parameters such as shape, number of components, and their orientation.[17−19] A key challenge is achieving delicate control over these morphological parameters through rational synthesis. A selected variety of achievable nanorod heterostructure (NRH) morphologies and some of the key factors influencing their formation are shown schematically in Figure 1. Reduced symmetry of the underlying

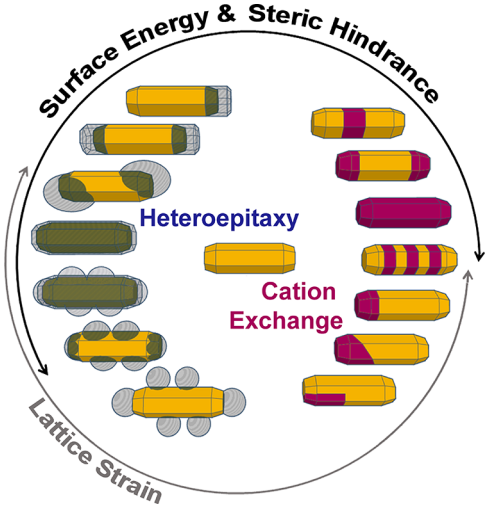

Figure 1. An overview of selected colloidal nanorod heterostructure morphologies and key parameters that control the growth modes.

crystal structure can differentiate nucleation and growth rates along different crystallographic directions, potentially allowing control over anisotropic growth. However, growth mechanisms are often a complex convolution of the varying enthalpies of terminating facets, which depend not only on the surface atomic arrangements but also on ligand chemistry and coverage, reactivity of precursors, and lattice strain, among many factors.

Heteroepitaxy and cation exchange have been explored most frequently for the synthesis of colloidal nanocrystal hetero-structures. Epitaxial growth in solution involves the sequential adsorption of cations and anions from molecular precursors onto the nanoparticle surface, which is often achieved through a modification or an extension of the seed nanocrystal synthesis conditions, *i.e.*, at high temperatures in nonpolar organic solvents, in which the semiconductor particles are suspended using amphiphilic ligands.[20] Cation exchange involves the change in composition of an already grown nanocrystal. Compared to heteroepitaxy, cation exchange reactions are carried out at lower temperatures, rely on differences in ligand affinity to the outgoing and incoming cations, and may leave the overall shape of the starting nanocrystals intact.[21] If starting from a homogeneous single-phase particle, partial cation exchange can be used to achieve two or more phases within.[22] Alternatively, cations of presynthesized heterostructures containing different anions can be exchanged.[23]

Solution heteroepitaxy to many anisotropic nanocrystal heterostructures can be considered to have emerged from an extension of the synthesis of colloidal semiconductor nanorods using concepts of thin film heteroepitaxy. It is well-known from thin film heteroepitaxy that uniform growth occurs when the surface energy of the substrate exceeds the sum of the surface and interfacial energies of the growing phase. This type of growth is known as the Frank−van der Merwe mode.[24] When the opposite is true, Volmer−Weber or island growth occurs. In many cases, Stranski−Krastanov growth mode can occur where initial uniform film growth converts to island growth due to the lattice mismatch causing strain build-up with increasing film thickness. In the solution-phase heteroepitaxy considered here, the substrate is the nanorod "seed" (for most examples discussed below) with different terminating facets that are passivated by organic ligands. The molecular precursors are typically the cation and anion complexed in solution by the same amphiphilic ligands which terminate the particle surface, which introduces a significant degree of complexity by affecting both the solubility of precursors and the steric hindrance to their adsorption.[25] This complexity can give rise to unique and intriguing morphologies that may be fine-tuned in a variety of ways with a deeper understanding of the growth mechanisms.

The asymmetry of the underlying wurtzite crystal structure has been an important factor in differentiating growth rates along different crystallographic directions for II−VI nanorods and NRHs. The symmetry of the underlying seed lattice varies the ratio of cations and anions at different surface terminations, which, along with the chemistry of the ligand's polar headgroup, determines the crystal-facet-dependent binding affinity, imparting regioselectivity in heterogeneous nucleation and growth. Of course, surface energies of the terminal facets are also strongly affected by ligand passivation and therefore the choice of ligands has been key in the synthesis of anisotropic nanocrystals as well as their heterostructures.

Because most crystalline materials will have different lattice parameters, the strain arising from this mismatch has important consequences on the regioselectivity and directionality of epitaxial growth. Lattice strain can vary across different crystallographic interfaces, favoring growth on certain facets over others and therefore dictating the number and location of secondary phase growth. Furthermore, it can impact the morphology of the growing phase. Lattice strain can cause growth with different aspect ratios, vary contact angles, and limit the size of the growing particles, similar to conventional heteroepitaxy on planar substrates.[26,27]

These three factors, *crystal structure*, *surface energies*, and *lattice strain*, may be considered as the fundamental thermodynamic parameters for the synthesis of colloidal nanorod heterostructures. That is, the crystal structure and the ligand binding affinity determine the surface energies of terminating facets for both the seed and the growing phases, which in turn vary the likelihood of certain facets undergoing heterogeneous nucleation and growth over others, imparting regioselectivity. Lattice strain can then dictate the morphology of the growing phase and, in some cases, even alter that of the seed.[27−31]

Kinetic parameters are just as critical to consider in NRH synthesis. Indeed, the anisotropic seed nanocrystals themselves are the results of kinetic control overriding the thermodynami-

https://doi.org/10.1021/acs.chemrev.2c00410
Chem. Rev. XXXX, XXX, XXX−XXX

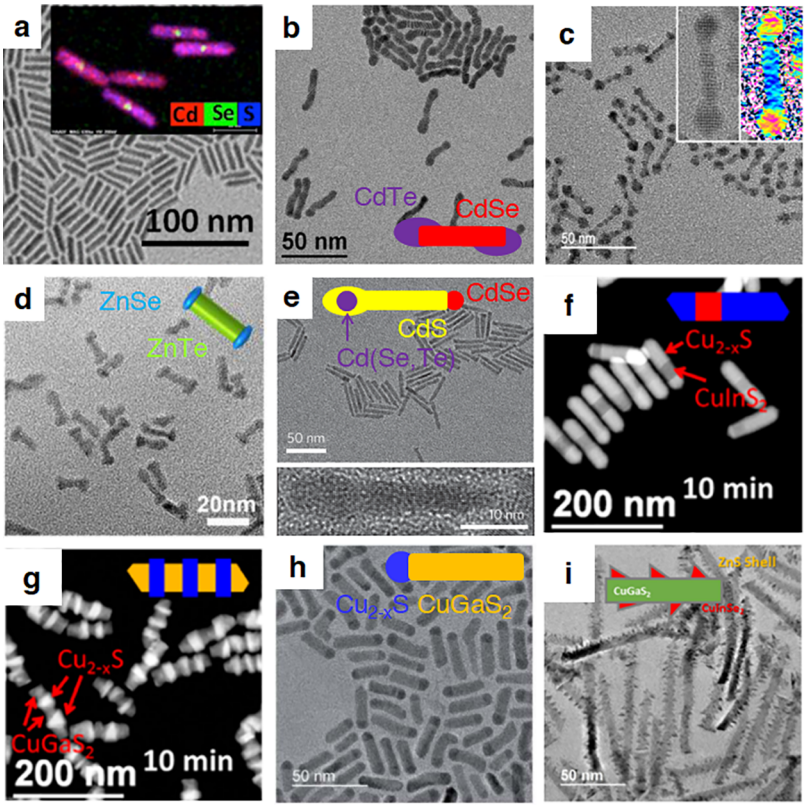

Figure 2. An overview of exemplary nanorod heterostructures. (a) CdSe/CdS dot-in-rods. Inset: energy dispersive X-ray map indicating the position of the CdSe cores.[51] (b) CdTe/CdSe/CdTe barbell structures with strain-induced curvature.[55] (c) CdSe/CdS/CdSe with ZnSe shell double heterojunction nanorods. Inset: Fourier-filtered distortion map indicating the position of the CdSe tips. (d) ZnSe/ZnTe/ZnSe barbells.[62] (e) Cd(Se,Te)/CdS/CdSe asymmetric barbell-like structures.[65] (f) $Cu_{2-x}S/CuInS_2$ nanorod heterostructures with single $CuInS_2$ segment from cation exchange.[42] (g) $Cu_{2-x}S/CuInS_2$ superlattice nanorods from cation exchange.[42] (h) $Cu_{2-x}S/CuInS_2$ single-tipped nanorods from concurrent seed growth and cation exchange.[71] (i) $CuInS_2$ nanorods with $CuInSe_2$/ZnS protrusions.[72] Schematic diagrams have been added to (b,e,h) for illustrative purposes. (e) Reproduced with permission from ref 65. Copyright 2013 Springer Nature. (h) Reproduced with permission from ref 71. Copyright 2021 Royal Society of Chemistry.

cally expected structures. *Precursor concentrations* and *reaction temperature* are perhaps the most rudimentary knobs with which to vary growth rates, but there are usually other kinetic factors that play important roles in imparting or enhancing anisotropic growth. Ligands can not only alter surface energies but also act as barriers for precursor or monomer diffusion to the surface of the seeds through *steric hindrance*.[32] The degree of steric hindrance is dependent on both the chain length and packing density, with the latter being determined by the surface cation density due to the underlying crystal structure as well as the structure of the ligand chains. This kinetic barrier strongly influences the regioselectivity and directionality, leading to anisotropic epitaxial growth. Furthermore, ligands are often a part of the precursors and can affect their *reactivity*, which in turn varies the availability or the concentration of the monomers and therefore the growth rate.[33,34]

Cation exchange can be an effective and a facile approach to achieving nanocrystal heterostructures because it exploits the high cation mobility in superionic conductors and the small diffusion lengths needed in nanostructures. Superionic conductivity,[35] defined as exceptionally high ionic mobility in a given substance, typically triggered by elevated temperature, has been known since 1914 when abnormally high conductivity was measured in α-AgI at high temperature.[36] In a superionic conductor, such as $Cu_{2-x}S$, cation mobilities can be on the same order as the self-diffusion constants of organic liquids.[37] Once the critical temperature has been reached (105 °C for Cu_2S[37,38] and 140 °C for Cu_2Se[39]), the cations can be thought of as a liquid within a rigid anion lattice. Choosing ligands in solution (or solvent molecules) with stronger affinity to the initial cations in the lattice than to the incoming cations can then easily drive the cation exchange reaction. Hence, unlike outward heteroepitaxy, cation exchange leads to inward nucleation and growth. Nevertheless, the same thermodynamic and kinetic factors discussed above for heteroepitaxy play key roles in determining regioselectivity and directionality.

The symmetry of the underlying lattice can differentiate cation diffusion rates along different crystallographic directions, contributing to directionality in phase conversion.[40] Varying surface energies of the terminating facets along with steric hindrance introduced by the adsorbed ligands can provide preference for nucleation on certain facets.[41,42] Ligands can also coordinate to the cations in solution, altering their reactivity and adding to the steric barriers.[40,41,43] The most stable interfaces are often the least strained ones and therefore the cation diffusion direction can be determined by the lattice strain, which in turn will define the number, size, and shape of the converted regions.[22]

Heteroepitaxy, cation exchange, and approaches combining both are beginning to enable a massive number of possible products, with widely ranging compositions and morphologies.

https://doi.org/10.1021/acs.chemrev.2c00410
Chem. Rev. XXXX, XXX, XXX−XXX

Much of the early efforts in the synthesis of anisotropic nanocrystal heterostructures have focused on solution-phase heteroepitaxy of II−VI compounds, building on the success of CdSe nanorod and tetrapod synthesis.[44−47] In particular, the earliest example of dot-in-rods,[48−50] which is formed by anisotropic heteroepitaxy of a CdS shell on a wurtzite CdSe quantum dot core, as shown in Figure 2a,[51] has received much attention for its quasi-type-II band structure, axially aligned dipole moment, and high photoluminescence quantum yield (PLQY). Barbells or dumbells have also been achieved through the growth of dots on both tips of a rod-shaped seeds. The barbell structures have been synthesized by solution heteroepitaxy for several compositions including CdTe/CdSe/CdTe,[52−59] CdSe/CdS/CdSe,[26,60,61] ZnSe/ZnTe/ZnSe,[62] and ZnSe/CdS/ZnSe,[63] shown in parts b, c, and d of Figure 2, respectively, for the first three examples. From the original development of these structures, a profusion of particle shapes and compositions are beginning to emerge. For example, these two strategies have been combined to form dot-in-rods with a different composition at one of the tips, such as the single CdTe-tipped CdSe/CdS dot-in-rods.[30,64] A similar asymmetric structure, the Cd(Se,Te)/CdS dot-in-rod with a single CdSe tip shown in Figure 2e, exhibits two-photon upconversion photoluminescence.[65,66]

Radial heterostructures can also be produced by heteroepitaxy on nanorod side facets. Due to the greatly increased interfacial areas involved compared to axial heterostructures, lattice strain can play a large role in determining the morphology of side facet growth. Relatively small lattice mismatch between CdS and ZnSe can yield relatively smooth conformal shells, while the larger lattice mismatch between ZnSe and ZnS converts to islands upon continued growth due to increasing strain as expected from the well-known Stranski−Krastanov growth mechanism.[27] Growth of CdSe on the sides of CdS nanorods leads directly to multiple islands without a noticeable prior conformal shell growth, presumably due to the higher surface energy and the lattice strain introduced by CdSe growth.[26] In a special case of ZnS growth on ZnSe nanords, helical shell growth around nanorods has also been observed to arise due to the balance between the lattice strain and surface energies.[27]

As advances in the development of anisotropic structures through heteroepitaxy continue, the discovery of facile cation exchange in nanocrystals is providing new avenues of exploration. Complex heterostructures achieved in II−VI compounds are now being converted to different compositions that otherwise do not yet have established synthetic routes with precise control over size and shape distribution. Zn- and CuIn-chalcogenide dot-in-rods have been produced by sequential cation exchange *via* Cu-chalcogenides while preserving particle morphology.[67,68] Cd/Zn II−VI barbell structures[23] with variable alloy composition have also been achieved through sequential cation exchange and significantly broaden the range of accessible colors and work functions for optoelectronic applications. Because exploiting cation exchange to convert II−VI anisotropic nanocrystal heterostructures to different compositions often requires intermediates such as Cu- or Ag-chalcogenides, efforts are currently being expanded in direct synthesis and conversion of these chalcogenides.[69,70] For example, partial cation exchange of $Cu_{2-x}S$ nanorods can lead to single- or multiply segmented NRHs (Figure 2f,g).[42] Concurrent or subsequent heteroepitaxy with cation exchange is providing additional dimensions to the synthesis of aniostropic nanocrystal heterostructures. Epitaxial growth of $Cu_{2-x}S$, concurrent with its conversion to I−III−VI_2 sulfides *via* cation exchange, has been shown to lead to single-tipped nanorods (Figure 2h).[71] Complete cation exchange of $Cu_{2-x}S$ to I−III−VI_2 sulfides, followed by solution heteroepitaxy of I−III−VI_2 and/or II−VI sulfides, has led to interesting morphologies of side-grown islands that are largely determined by lattice-mismatch-induced strain (Figure 2i).[72]

Despite the rapidly expanding number of compositions and morphologies in nanocrystal heterostructures, the understanding of the growth mechanisms and therefore the control over the shape, size, and location of the added or exchanged phases can be difficult to achieve and are often considered on a case-by-case basis. Due to the complexity of the anisotropic shape and the chemistry, concepts elucidated from one system do not always apply straightforwardly to another. In this review, we attempt to connect various insights gained from prior research efforts to highlight arguably the most important design principles that must be considered in developing novel nanorod heterostructures. We focus on the synthesis of heterostructures of colloidal semiconductor nanorods, the simplest and the most widely accessible of anisotropic shapes.[17−19] Particular attention is given to the growth mechanisms, which shed light on how different thermodynamic and kinetic parameters impart regioselectivity in heteroepitaxy and cation exchange processes. Given that most of the efforts in this area have been within II−VI and $Cu_{2-x}S$-based heterostructures, examples from these two families of materials are discussed in the following sections. Selected application prospects of colloidal NRHs are then discussed.

2. SOLUTION EPITAXIAL GROWTH OF II−VI NANOROD HETEROSTRUCTURES

Each of the above-mentioned thermodynamic (crystal structure, surface/interface energies, and lattice strain) and kinetic (precursor reactivity, ligand steric hindrance, precursor concentration, and reaction temperature) factors plays an important role in the solution epitaxial growth of nanorod heterostructures. Their contributions to the growth mechanisms are discussed further with selected examples from the literature with respect to heteroepitaxial growth of II−VI NRHs in this section. Broadening the composition space of these NRHs through cation exchange is then briefly considered, with further discussion on this topic continued in the subsequent section.

2.1. Thermodynamic Factors

2.1.1. Crystal Structure and the Terminating Facets. The shape of a nanocrystal is deeply tied to its crystallographic phase. In II−VI nanocrystals, CdSe and CdS, in particular, the ability to synthesize both zinc blende and wurtzite phases, has been especially enabling in heterostructure synthesis. This polytypism allows the exploration of crystal structure effects within the same composition. The prototypical example is the difference between dot-in-rods and tetrapods. When starting with nearly "spherical" nanocrystals, zinc blende seeds can lead to the growth of 4 equivalent pods into the tetrapod structure. Tetrapod heterostructures of several different combinations of compositions have been achieved with zinc blende seeds (*e.g.*, CdSe, CdTe, ZnTe, $CuInS_2$, and InP) and wurtzite pods (*e.g.*, CdS, CdSe, CdTe, ZnS).[47,73,74] On the other hand, wurtzite

https://doi.org/10.1021/acs.chemrev.2c00410
Chem. Rev. XXXX, XXX, XXX−XXX

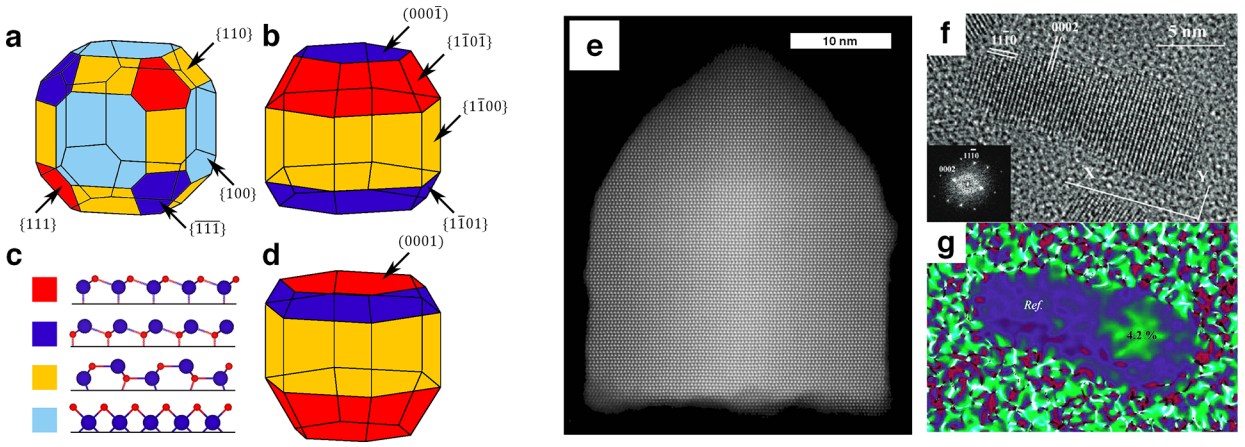

Figure 3. Low-index surface planes of zinc blende (a) and wurtzite (b,d) particles. The termination of each facet is indicated by color, represented in (c), where large blue atoms are anions and small red atoms are cations. TEM micrographs of a bullet-shaped low aspect ratio wurtzite CdS particle (e)[79] and CdSe/CdS dot-in-rod (f) exhibiting anisotropic shape.[50] The location of the CdSe core is indicated by a color-coded dilation map (g),[50] the scheme of which has been altered here for accessibility.

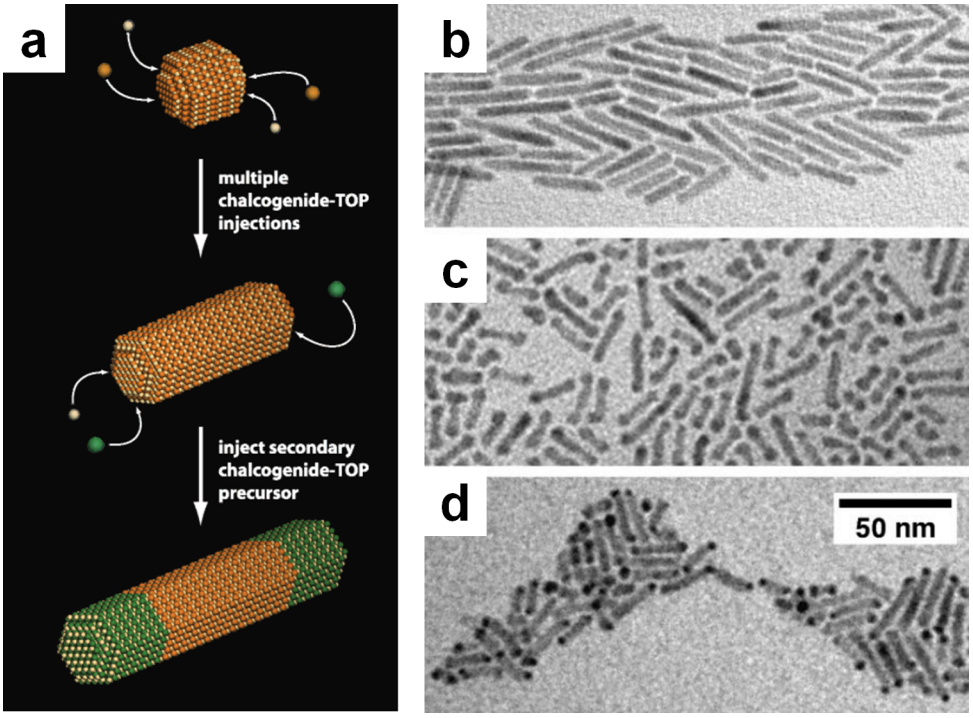

Figure 4. (a) Schematic showing a strategy for nanorod heterostructure synthesis through multiple injections extending rod growth. Addition of a second precursor source leads to a second composition grown at the tips.[84] TEM images of seed CdS nanorods (b) growing into CdTe/CdS/CdTe barbells (c) through a similar approach, followed by regioselective deposition of Au on their tips (d).[85] (b–d) Reproduced with permission from ref 85. Copyright 2006 Royal Society of Chemistry.

seeds lead to the dot-in-rod structure with a rod-shaped shell growing along the *c*-axis of the crystal, with CdSe dot in CdS rod being most widely studied.[32,50,51,75−77] Of course, there are exceptions such as twinned wurtzite CdTe seeds leading to tetrapod growth.[78]

Whether heterogeneous nucleation occurs in four directions as in tetrapods or in two opposite directions as in dot-in-rods depends strongly on the terminating facets of the seed, which is determined by the crystal phase. Considering only the low-index planes, zinc blende particles can terminate with anion-terminated $(\overline{111})$, cation-terminated (111), cation-terminated {100} that have twice the dangling bonds per atom, and/or mixed cation−anion terminated {110} planes as shown in Figure 3a. The side view of the atomic arrangement of each termination facet is represented in Figure 3c, where large blue atoms are anions and small red atoms are cations. Then it can take the shape of a tetrahedron, cube, octahedron, or a truncated form that is a combination of these shapes with the lowest energy facets dominating the surface area. While the highest planar density facets may be expected to minimize dangling bonds, the actual surface energy will be strongly dependent on the nature of ligand passivation, which is considered in the next subsection. Nevertheless, this crystal symmetry tends to lead to the formation of tetrapods with wurtzite pods, which are grown on the four high energy facets of a zinc blende seed.[47,50,73,74] This special zinc blende/

https://doi.org/10.1021/acs.chemrev.2c00410
Chem. Rev. XXXX, XXX, XXX−XXX

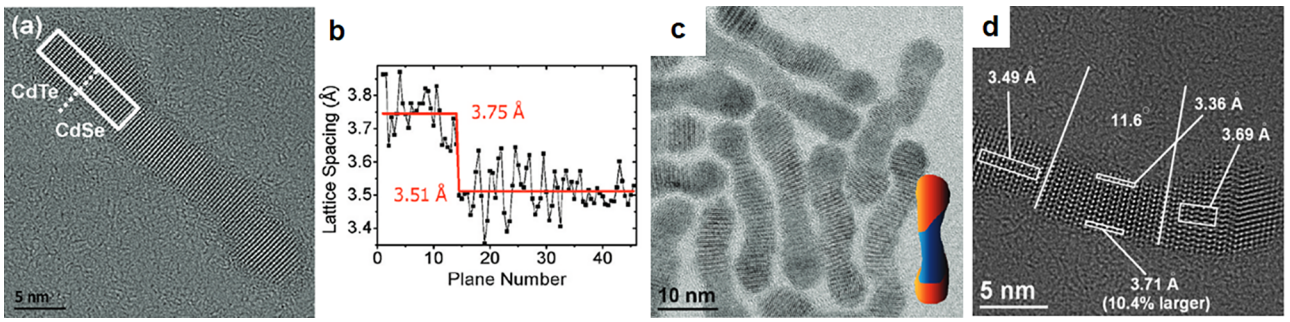

Figure 5. (a) High-resolution TEM image of a linear CdTe/CdSe/CdTe barbell nanorod heterostructure. (b) Corresponding lattice spacing across the heterointerface indicated by the dashed line in (a).[28] (c,d) Curved CdSe/CdTe nanorod heterostructures, arising from partial side growth of CdTe and the large lattice mismatch between the two phases.[28,55]

wurtzite phase boundary occurs as a result of thermodynamic conditions that favor growth of the wurtzite phase and the matching termination of the zinc blende $(\bar{1}\bar{1}\bar{1})$ and the wurtzite $(000\bar{1})$ facets as indicated by the color coding in Figure 3a−d.

Again, considering only the low-index planes, wurtzite particles with lower symmetry can have mixed anion−cation terminated $\{1\bar{1}00\}$, cation-terminated (0001) and $\{1\bar{1}0\bar{1}\}$, and/or anion-terminated $(000\bar{1})$ and $\{1\bar{1}01\}$ facets as shown in Figure 3b,d. Wurtzite particles can then adopt a (truncated) hexagonal prism, conic, or bullet shape (Figure 3e) to minimize surface energy. The cation- and anion-terminated facets are of particular importance to heteroepitaxy, and it is the asymmetry between the (0001) and $(000\bar{1})$ facets of wurtzite and the resulting difference in ligand passivation that gives rise to linear growth leading to the dot-in-rod structure (Figure 3f). It can be seen from the lattice fringes and Fourier transform (similar to a diffraction pattern) in the inset of Figure 3f that the wurtzite lattice is maintained across the CdSe/CdS interface. This asymmetry is also the reason why the predominant anisotropic nanocrystal heterostructures achieved to-date are nanorod-based structures.

2.1.2. Ligand Passivation and Surface Energies. While the underlying crystal structure can strongly influence which terminating facets are favored and the overall geometry of the seed particle, ligands are often the key to anisotropic heterostructure growth through passivation of dangling bonds and modification of surface energies. For example, the dot-in-rod structures are achieved because the side $\{1\bar{1}00\}$ facets of the wurtzite seeds are where the phosphonic acid ligands are strongly bound and reduce surface energy.[80−82] Hence, radial growth is suppressed. The dynamic nature of the bonds between ligands, precursor ions in solution, and the particle surface is critical. The binding affinity in each of these cases depends strongly on the selected chemistry, temperature, and concentrations involved. We note that there are also kinetic factors that enhance asymmetric growth, in particular steric barriers for precursor diffusion to the surface, which are discussed later. Because these ligands preferentially bind to cations,[80−83] nucleation, and growth on the anion-terminated $(000\bar{1})$ facet is usually much faster than the cation-terminated (0001) facet, as exemplified by the dot-in-rod shown in Figure 3g, where the seed dot is located near one end rather than at the center of the rod. Here, the Fourier transform of the lattice fringes (Figure 3f inset) is used to generate a dilation map, where deviation from the CdS lattice parameters is visualized to locate the larger lattice CdSe in Figure 3g.[50]

Heterostructures grown starting from a nanorod seed perhaps illustrate this ligand effect more drastically. The earliest heterostructures grown from nanorod seeds reported were rod/rod/rod or barbell structures.[52,84−87] Such structures can be achieved simply through a change of precursor in an existing seed reaction that already favors rod growth. For example, the direct addition of Te precursors to a reaction mixture of CdSe nanorods with excess unreacted Cd precursors can easily lead to CdTe/CdSe/CdTe rod/rod/rod structures (Figure 4).[84,85] Here, the key ingredient in the initial seed rod is the long chain phosphonic acid that binds more strongly on the side $\{1\bar{1}00\}$ facets and imparts preferential growth along $[000\bar{1}]$ direction, leading to rod growth, which is extended during the second phase growth with a change from Se to Te precursors. That is, when the chosen ligands reduce the surface energy of the side facets more than the tip facets, tip growth dominates. Similar to dot-in-rods, heteroepitaxy on the anion-terminated $(000\bar{1})$ plane is often much faster than on the cation-terminated (0001) plane, leading to asymmetric tip lengths as has been shown for CdSe/CdS/CdSe rod/rod/rod structures.[60]

It should be noted that wurtzite nanorods of CdSe and CdS can exhibit pronounced tapering at the $(000\bar{1})$ end. An extreme case is the bullet shaped nanorod shown in Figure 3e, but it is also evident in the dot-in-rod of Figure 3f. This shape arises from stabilizing cation-terminated $\{10\bar{1}\bar{1}\}$ facets and/or providing steric hindrance to precursor diffusion with ligands. A similar effect is seen in arrow and teardrop shaped nanorods.[44] This "tapering" effect has also been exploited to synthesize dual diameter dot-in-rods.[32]

When the choice of ligands leads to an insufficient difference in the surface energies among the terminating facets for a given reaction condition, that is, no significant preference for tip growth for the seed nanorods, core/shell structures can be expected. In the case of CdSe/ZnS NRHs exhibiting uniform heteroepitaxy, the CdSe nanorod cores were first recapped with alkylamines prior to shell growth.[88] In the case of ZnSe/ZnS, alkanethiols (which also act as S source) and excess alkylamine or a combination of excess alkylamine and carboxylic acid were utilized to grow a uniform shell.[89] Hence, amines and potentially other ligands that either bind relatively weakly on the surface of seed nanocrystals or bind without a significant preference to certain facets appear to promote uniform shell growth.

2.1.3. Lattice Strain. In heteroepitaxy, lattice mismatch leading to strain is frequently one of the most important determinants of morphology and can cause dislocations to arise in thin film growth. Surprisingly, for tip-only growth on

https://doi.org/10.1021/acs.chemrev.2c00410
Chem. Rev. XXXX, XXX, XXX−XXX

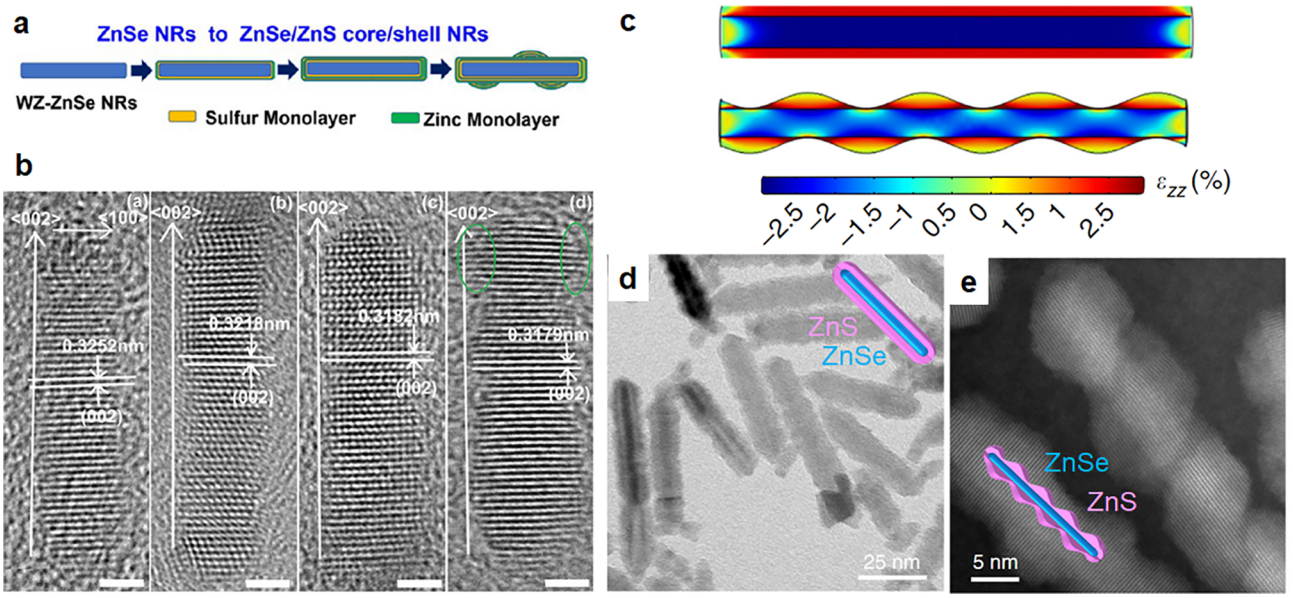

Figure 6. (a) Scheme illustrating the ZnS shell growth mechanism on the sides and tips of wurtzite-ZnSe NRs.[89] (b) TEM images of ZnSe nanorod (left) and ZnSe/ZnS rod/shell NRHs with increasing shell thickness (left to right). Scale bars are 2 nm.[89] (c) The calculated elastic strain tensor ϵ_{zz} of a ZnSe nanorod with a flat or helical ZnS shell.[27] TEM imgages of isotropic (d) or helical (e) shell growth of ZnS on ZnSe nanorods using low or high excess oleic acid, respectively.[27]

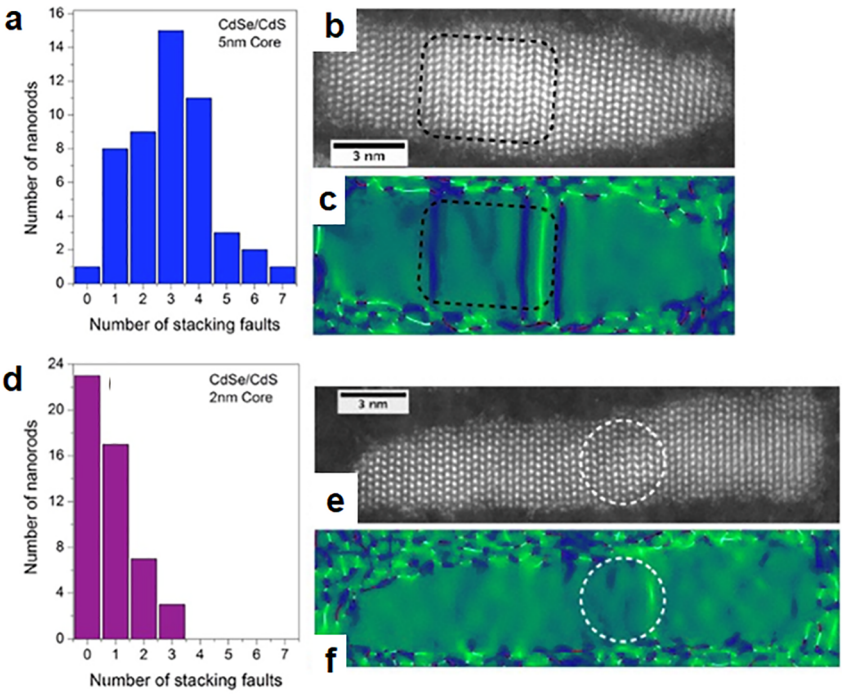

Figure 7. Distribution of the number of stacking faults (a,d), high-angle annular dark field STEM images (b,e), and the corresponding strain maps (c,f) for CdSe/CdS core/shell NRHs with 5 nm cores (a−c) or 2 nm cores (d−f).[29]

colloidal nanorods, reports of lattice mismatch effects on the resulting structure are sparse. For example, despite 7% mismatch in their corresponding bulk lattice parameters, the CdTe/CdSe junction exhibits essentially an atomically sharp transition from CdTe lattice spacing along [0001] direction to that of CdSe across the interface in CdTe/CdSe/CdTe barbell heterostructures as shown in Figure 5a,b.[28] Thus far, it is only when CdTe growth extends beyond the tips to the sides of the seed CdSe nanorods that lattice strain has been observed to play a critical role in the morphology and the resulting optical properties of these nanorod heterostructures. In this example of CdTe/CdSe/CdTe heterostructures, a significant overgrowth of the CdTe tips to the sides of the CdSe rod leads to an unusual bending of the seed nanorods. It is the strain due to the larger CdTe lattice that causes the bending. As evidenced by the change in the local lattice spacings, this bending results in large tensile and compressive strain at the outer and inner parts of the curvature, respectively, in the CdSe seed rod as shown in Figure 5c,d.[28,55]

https://doi.org/10.1021/acs.chemrev.2c00410
Chem. Rev. XXXX, XXX, XXX−XXX

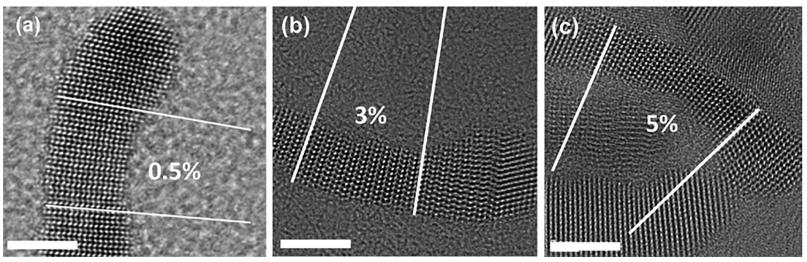

Figure 8. High-resolution TEM images of CdSe/CdTe NRHs of increasing strain. Diameter of seed CdSe nanorods decreases from (a) to (c), and the estimated compressive strain is indicated in each image. Scale bars are 5 nm.[28]

When the ligand choice and other reaction conditions allow side (and tip) growth, a uniform shell with strain-dependent morphology has been reported. In the ZnSe core/ZnS shell NRHs, the first few layers (~two monolayers) of ZnS grow as a uniform shell.[89] However, as growth continues, islands form on the surface of the NRHs (Figure 6a,b). Much like the Stranski–Krastanov growth mechanism in thin film heteroepitaxy, these observations have been attributed to the buildup of lattice strain arising from the lattice mismatch between ZnSe and ZnS (4.5% based on bulk lattice parameters). To accommodate this strain, growth on the three-dimensional substrate that is a nanorod can take the form of periodically spaced protrusions or even a helix (Figure 6c–e). Here, ZnSe termination leads to higher surface energy, while increasing coverage of the ZnS surface induces more strain. The manifestation of the helical shell morphology is attributed to a compromise between these two factors to minimize energy. The critical thickness for the transition from uniform shell to island growth in NRHs has been shown to decrease with increasing lattice mismatch for ZnS growth on ZnSe, CdS, and CdSe nanorods.[27]

The effects of lattice strain are expected to depend on the size of both the seed and the shell. In the CdSe/CdS dot-in-rod system, the number of planar defects has been suggested to be dependent on the seed size.[29] Figure 7 compares dot-in-rods with either small (~2 nm diameter) dot or larger (~5 nm diameter) rod-like cores. The strain images (Figure 7c,f) reveal stacking faults that are perpendicular to the long-axis of the rod, which presumably relieve the strain arising from lattice mismatch. The number of stacking faults per nanorod distribution plots (Figure 7a,d) reveal that the larger core results in a larger number of such defects. This effect has been rationalized by considering that the smaller seed can be more easily deformed to allow a more perfectly crystalline shell to be grown around it.[29]

In the case of CdSe/CdTe NRHs mentioned earlier where CdTe tip growth extends to the sides of the seed CdSe rod, the degree of bending, rather than the number of defects, varies with the seed rod diameter. In Figure 8, such NRHs with three different seed CdSe rod diameters are shown.[28] As the diameter decreases, the radius of curvature decreases, leading to increasing compressive strain at the inner part of the curvature. A very large compressive strain of 5% for the smallest diameter case shown has been estimated based on the difference in the lattice spacing compared to a separate single-phase CdSe rod. Unlike the dot-in-rod case mentioned above, bending rather than defect formation accommodates the lattice-mismatch-induced strain. Nevertheless, it is the same rationale that leads to the observed size dependence. That is, smaller diameter allows the seed rod to be more easily deformed, leading to a larger degree of bending.

The examples of the roles of lattice strain in NRH synthesis discussed above have been limited to cases where the lattice mismatch is the dominant factor to emphasize its consequences without the complication of other parameters. Ultimately, it is the minimization of the overall energy of the system for a given reaction condition that determines the structure/morphology of the resulting NRHs. Even before considering kinetic parameters (some of which are discussed in the next section), the balance of different thermodynamic factors has been shown to yield a variety of interesting morphologies.

2.2. Kinetic Factors

2.2.1. Precursor Reactivity. Whether the heteroepitaxy on seed nanorods is in the reaction- or diffusion-limited regime will greatly alter the resulting morphology of NRHs. In principle, which regime a given reaction is in may be decided by the reactivity and the concentration of the precursors for a fixed reaction temperature. In most II–VI nanocrystal synthesis, the reactivity of a metal precursor is often determined by the ligands present because metal–ligand complex formation occurs prior to the nucleation and growth of the nanocrystal.[25] Hence, varying ligand chemistry may provide insights on how precursor reactivity affects NRH morphology. However, ligands can also alter many other parameters in NRH growth. As discussed earlier, the same metal–ligand bond that forms the precursor metal complexes in solution plays a critical role in determining the surface energy of different terminating facets of the seed nanocrystal, which in turn strongly influences how heterostructures nucleate and grow. Ligands also establish the steric barrier for precursor diffusion at the surface of the nanocrystal which, in some cases, can be the dominating factor in determining the morphology of the resulting NRHs as discussed later. Hence, it is difficult to separate out the effects of precursor reactivity from other effects.

Reagent concentrations are, however, frequently varied to control and optimize nanocrystal synthesis. In particular, varying metal-to-ligand ratio in heteroepitaxial growth can have a significant impact on the morphology and/or composition of NRHs without varying the chemistry of surface-bound ligands. One such example is in ZnS shell growth on ZnSe nanorods mentioned earlier. By varying the Zn-to-oleic acid ratio, the ZnS shell can be tuned from a nearly uniform shell to a helical shell (Figure 6c–e).[27] A nearly uniform shell forms at the highest Zn-to-oleic acid ratio of 1:4, island growth is observed at intermediate Zn-to-oleic acid ratios, and a helical shell occurs at the lowest ratio of 1:10. The increasing oleic acid concentration increases Zn precursor solubility, making Zn less available or effectively less reactive for shell growth. The reduced reactivity allows the shell growth to balance the

https://doi.org/10.1021/acs.chemrev.2c00410
Chem. Rev. XXXX, XXX, XXX–XXX

surface and strain energies, leading to the lowest-energy helical configuration in the reaction-limited regime.

Varying the Zn-to-oleic acid ratio has also revealed a surprising etching effect during NRH synthesis. It has been shown that oleates (not limited to Zn-oleate) can cause anisotropic etching of CdS nanorods and CdSe/CdS/CdSe barbells, where faster etching rates are seen at the tips.[26] Upon addition of Se precursor after etching, regrowth can occur both at the tips and on the sides of the nanorods. The dots that are grown on the sides of the initial CdS nanorods anisotropically etched by Zn-oleate are Cd-rich (Cd, Zn)Se (Figure 9a)

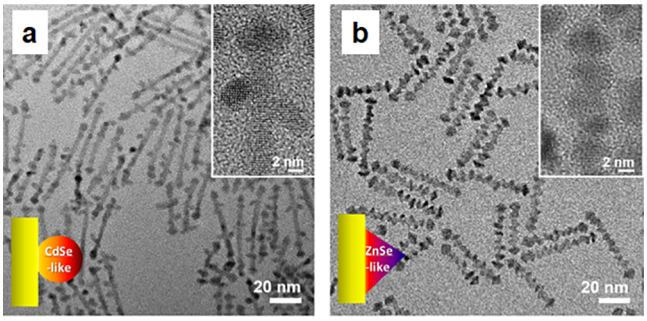

Figure 9. Distinct modes of island growth on CdS nanorods with Cd-rich (a) or Zn-rich (b) (Cd,Zn)Se dots exhibiting high and low contact angle growth, respectively.[26]

despite the fact that the reaction mixture contained an excess amount of Zn-oleate. When the same etching and regrowth reaction is carried out with increasing amount of oleic acid (Zn-to-oleic acid ratio from 1:2 up to 1:12), the composition of the side-growing dots changes to Zn-rich (Cd,Zn)Se along with decreasing contact angle (Figure 9b). Here, the excess oleic acid can now increase the solubility of the etched Cd, allowing Zn to better compete during regrowth.[26] A similar effect can be achieved by adopting a hot injection procedure to quickly grow ZnSe before Cd-oleate can be generated *in situ*.[61]

While the above examples focused on metal precursor reactivity, because the product is a compound semiconductor, the effects of ligands on precursor reactivity are further complicated when anion precursors are also considered. For example, while excess carboxylic acid can reduce the metal reactivity by stabilizing the metal−carboxylate complex in solution,[25] it can also increase the reactivity of the chalcogen through protonation of the phosphine chalcogenide precursors to form highly reactive dihydrogen chalcogenides.[34] Many efforts focused on elucidating such ligand effects on precursor reactivity have provided important insights on homogeneous nucleation and growth of nanocrystals[25,34] and it appears timely to expand on these studies to heteroepitaxial growth of NRHs and other more complex structures.

2.2.2. Ligand Steric Hindrance. Another important role ligands play in the synthesis of NRHs is providing a steric barrier for monomer diffusion at the surface of the nanorods. The chain length of ligands strongly influences diffusion of monomers to the particle surface by altering the permeability of the ligand shell as illustrated in Figure 10a. While a variety of ligand lengths are available, the effective permeability of the ligand shell can be tuned by using mixtures of ligands with different chain lengths. The relative permeabilities of ligand shells for a few low-index facets are plotted in Figure 10b for an octadecylphosphonic acid (ODPA)/hexylphosphonic acid (HPA) mixture. By varying the ODPA fraction and precursor feed rate, controlled asymmetry of the rod length and diameter has been achieved in CdSe/CdS dot-in-rods.[32]

At high ODPA fraction, the $(000\bar{1})$ is much more permeable than other facets and therefore rod growth occurs on this facet with very little to no growth on the cation-terminated (0001) side of the rod. The initial "tapering" at the $(000\bar{1})$ tip of the rod may be attributed to the cation-terminated $\{1\bar{1}0\bar{1}\}$ facet, which may be expected to have comparable stability to the (0001) termination. This can lead to the growth of a smaller diameter CdS rod. Hence, it appears that ODPA induces selectivity *via* steric hindrance to impede monomer diffusion to the surface on all other facets, much more so than on the $(000\bar{1})$ tip.

As the ODPA fraction decreases, both tips grow, with the $(000\bar{1})$ end being smaller diameter and the (0001) side growing with approximately the same diameter as the original seed. The shorter HPA likely facilitates monomer diffusion to the (0001) and $\{1\bar{1}0\bar{1}\}$ surfaces due to disrupting interactions between ODPA and having weaker van der Waals interaction between alkyl chains per molecule than ODPA. Single diameter rods are achieved with low monomer concentrations, which facilitates growth favoring replacement of the $(000\bar{1})$ with the lower energy $\{1\bar{1}0\bar{1}\}$ facets, as schematically illustrated in Figure 10c. As shown in Figure 10b, the permeability of these facets to monomer diffusion is more comparable to that of the (0001), leading to symmetric growth. Under conditions of high monomer concentration, the fraction of ODPA still determines whether growth is preferential on the $(000\bar{1})$ end (high ODPA fraction) or on both ends (low ODPA fraction). Some of these results are summarized in Figure 10d−g. Concepts related to the effects of different chain length alkyl phosphonic acids and ligand mixtures have also been explored in the synthesis of initial single-component[45,46,90] and heterostructured[50,85,87] nanorods.

2.2.3. Precursor Concentration and Reaction Temperature. The most accessible reaction parameters that can be varied in NRH synthesis are precursor concentration and reaction temperature. The main effect of precursor concentration is to push the equilibrium by mass action thereby altering reaction rates. Reaction temperature provides the thermal energy to overcome the barriers due to thermodynamic and kinetic factors, some of which have been discussed above. Hence, while these parameters are easy to vary, predicting the outcome is nontrivial as they will impact all factors simultaneously.

An insightful example with respect to precursor/ligand concentration effects on NRH growth has been given by Cossairt *et al.*[91] As nanorod growth occurs, the depletion of precursors can eventually lead to a transition from 1D to 3D growth, causing reduction in the aspect ratio. 1D growth can be sustained by continued addition of precursors. Adding free ligands can have the opposite effect, decreasing the reactivity of the precursor and causing a transition from 1D to 3D growth by shifting the equilibrium to favor, for example, complexation of metal ions by ligands in solution. This effect is qualitatively demonstrated in Figure 11, in which increasing concentration of ODPA ligands, while holding Cd ion concentration constant, leads to decreasing length and increasing diameter of the resulting CdS nanorods. Therefore, varying both the overall concentration of precursor in solution as well as the relative concentration between precursor ions and ligands

https://doi.org/10.1021/acs.chemrev.2c00410
Chem. Rev. XXXX, XXX, XXX−XXX

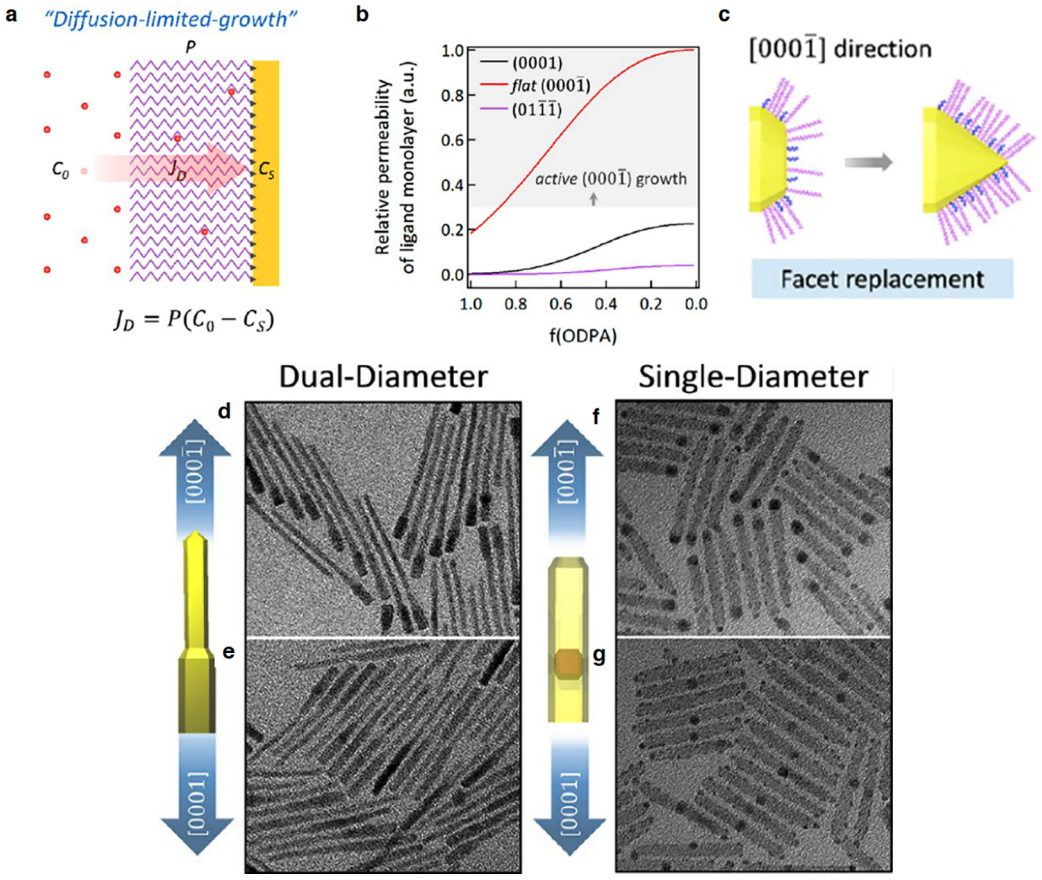

Figure 10. (a) Schematic of growth where monomer supply is limited by the surface ligand steric barrier. Diffusion flux of monomers (J_D) through the ligand layer is given by the product of the permeability coefficient (P) and the difference in monomer concentration in the bulk (C_0) and at the surface (C_S).[32] (b) Dependence of the estimated relative permeability of the ligand layer at (0001), (000$\bar{1}$), and {1$\bar{1}$01$\bar{1}$} surfaces of wurtzite CdS on ODPA fraction, f(ODPA).[32] (c) Schematic showing the replacement of (000$\bar{1}$) tip termination with {1$\bar{1}$01$\bar{1}$} facets at low monomer concentrations. TEM micrographs of dual-diameter CdS nanorods grown using high (d) or low (e) ODPA fraction. TEM micrographs identifying the core position of CdSe/CdS dot-in-rods grown using high (f) or low (g) ODPA fraction through preferential deposition of gold at the core position.[32]

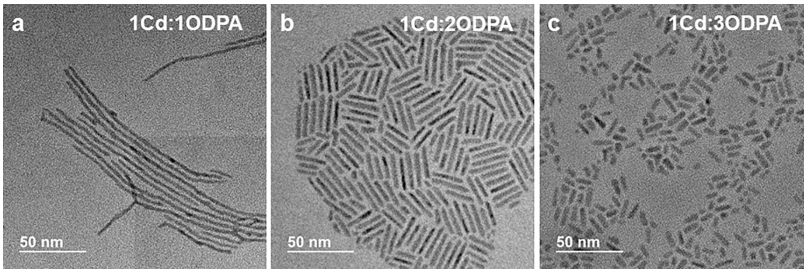

Figure 11. CdS nanorods grown using the indicated ratios of Cd to octadecylphosphonic acid (ODPA) and otherwise identical conditions.[92]

provides a readily accessible route to controlling axial *versus* omnidirectional growth of NRHs.

One interesting case of using reaction temperature to influence thermodynamic *vs* kinetic growth can be seen in CdTe/CdSe/CdTe barbell nanorods. Given a reaction condition that initially favors 1D tip growth of CdTe on CdSe nanorod seeds (Figure 5a), increasing the reaction temperature by 50 °C allows the growth to extend partially to the side facets of the seed nanorods (Figure 5c,d). The partial side growth induces a striking lattice strain effect that leads to unusual bending of the seed nanorods as shown in Figure 8.

Reaction heating rate can also have a significant impact on the morphologies of NRHs. For example, (Cd,Zn)Se can be grown on both the sides and tips of CdSe/CdS/CdSe barbells or exclusively on the tips by varying the heating rate (Figure 12).[61] Here, when the barbell NRHs are placed in the reaction mixture with Zn-oleate and slowly heated with dropwise addition of Se precursor, side growth is promoted (Figure 12a).[61] Interestingly, ZnSe grown on CdSe/CdS/CdSe barbell nanorods appears to be quite similar to the ZnSe/ZnS helical shell NRHs (Figure 6c–e).[27] When the barbell NRHs are injected with Se precursor into a solution of Zn-oleate at a high reaction temperature, tip growth without significant side growth is observed (Figure 12b).[61] Swift coinjection of seed particles and shell precursors at high temperature can be considered as the upper limit of the heating rate. While the different composition of the tip (CdSe) compared to the main rod (CdS) contributes to the preferential increase in the tip

https://doi.org/10.1021/acs.chemrev.2c00410
Chem. Rev. XXXX, XXX, XXX−XXX

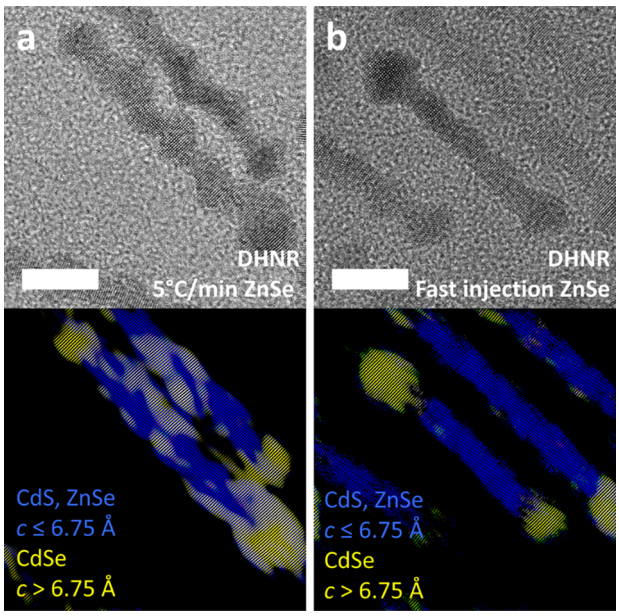

Figure 12. High-resolution TEM and the corresponding inverse Fourier-filtered images of CdSe/CdS/CdSe barbell-shaped NRHs (also referred to as double-heterojunction nanorods, DHNRs) with (Cd,Zn)Se final shell grown using heat up (a) or fast injection (b). scale bars are 10 nm. The false-color scale identifies different compositions through differences in lattice parameter range. Reproduced with permission from ref 61. Copyright 2019 AIP.

reactivity, in this particular case, the slow heating rate exposes the NRHs to selective etching and regrowth process discussed earlier, while the fast injection circumvents this effect.

2.3. Conversion of Nanorod Heterostructures *via* Cation Exchange

Consideration of above-discussed factors in epitaxial growth of complex NRHs can result in strategies for designing highly specific experimental approaches for tailored morphologies of NRHs. While the underlying concepts should indeed be broadly applicable, adapting synthetic protocols for one set of compositions to achieve identical geometries for a set of different compositions is not straightforward. Differences in preferred crystal structure, facet-dependent ligand passivation/surface energies, lattice mismatch, and the reactivities of available precursors will all be different and therefore need to be empirically optimized. While emerging artificial intelligence techniques exploring the reaction parameter space may drastically accelerate such an empirical approach,[93−95] there is no guarantee that a feasible condition can be found for a given morphology and composition using available ligands and precursors. For example, an inherently different lattice mismatch can make a unique morphology achieved for one composition energetically unfavorable for another.

Chemical conversion of an accessible particle structure to another set of compositions while retaining the morphology *via* cation exchange is then an interesting and promising route. While the nascent nature of this approach to heterostructures limits the number of examples, there are some promising results that demonstrate its utility. A complicated yet well-established synthesis of Cd chalcogenide-based NRHs may be converted to produce other compositions. Two such examples and their strategies are outlined in Figure 13. We refer the readers to more in-depth and general review articles on cation exchange of II−VI nanocrystals[21,96] and highlight a few important concepts for NRHs here and discuss cation exchange of $Cu_{2-x}S$ nanocrystals further in the next section.

For the single cation exchange of CdSe/CdS dot-in-rods shown in Figure 13a, the first step is the exchange of Cd to Cu, which is accomplished by the addition of Cu(I) to the seed heterostructure nanorods. Following complete exchange, the $Cu_{2-x}Se/Cu_{2-x}S$ dot-in-rod intermediate can then be converted back into a II−VI NRH with a different cation, in this case, as ZnSe/ZnS[67] shown in Figure 13b−g or to other compositions such as $CuInSe_2/CuInS_2$.[68] One of the key challenges in the sequential cation exchange approach lies in the difficulty of fully extracting Cu ions during the second exchange step and therefore leading to potential Cu(II) impurities resulting in defect emission.[97,98] Even an average of one copper atom per nanocrystal can in principle result in substantial reduction of PLQY. A successful synthesis of Zn and/or Cd chalcogenide heterostructures with suppressed deep trap recombination and efficient band edge PL is accomplished by the application of amines and phosphines,[23,67,98] which in sufficient excess, with time and/or elevated temperature, can efficiently extract Cu ions.

In addition to complete exchange of one cation for another, mixed precursors can be used in the second exchange step to achieve alloying. Figure 13i shows the final result of exchanging CdSe/CdS/CdSe barbells that have first been converted into an intermediate of $Cu_{2-x}Se/Cu_{2-x}S/Cu_{2-x}Se$ with a final mixture of Cd^{2+} and Zn^{2+}. For nanorods, the use of methanol as a solvent and preferential ligand for Cd ion extraction can unfortunately cause severe aggregation of the nanorods in the first step of exchanging Cd with Cu, leading to complications in both the overall cation exchange process and characterization of the products. The use of Cu(I)-oleate in the absence of methanol has mitigated this issue.[23] Furthermore, similar to the differences in precursor reactivity that arise in heteroepitaxy, different cations have different binding affinities for ligands and the anions on the surface of the lattice. The composition within the final product will therefore not match the feed ratio of cations in the second exchange step with mixed cation precursors. To address this problem, alkyl thiols were added to bind to Cd in solution, more closely balancing the effective affinities of Cd and Zn, enabling exchange of barbells to a variety of compositions with band gaps spanning the visible range as shown in Figure 13j,k.[23] Interestingly, the exchange of mixed cations leads to different Cd/Zn ratios in the two phases of the heterostructures. The EDX map of Zn and Cd in Figure 13i indicates a greater concentration of Zn in the sulfide rod and Cd in the selenide tip. A likely explanation is the difference between the solubility product constants K_{sp} of the possible product compounds CdS, CdSe, ZnS, and ZnSe, with lower K_{sp} indicating a more stable solid phase. In this system, solid CdS and CdSe are favored over their Zn counterparts but the difference in K_{sp} between CdSe and ZnSe is larger than that between CdS and ZnS. Hence while there is more Cd than Zn throughout the nanorod, the larger difference in K_{sp} leads to more Cd being present in the selenide tips compared to the sulfide rod. While each anion lattice region also presents different surface facets through which cation exchange may occur, control experiments using single-phase nanorod seeds resulted in compositions similarly biased toward either of these two compounds.[23]

As exemplified by both dot-in-rod and barbell structures discussed above, the choice of ligands and solvents is critical to

https://doi.org/10.1021/acs.chemrev.2c00410
Chem. Rev. XXXX, XXX, XXX−XXX

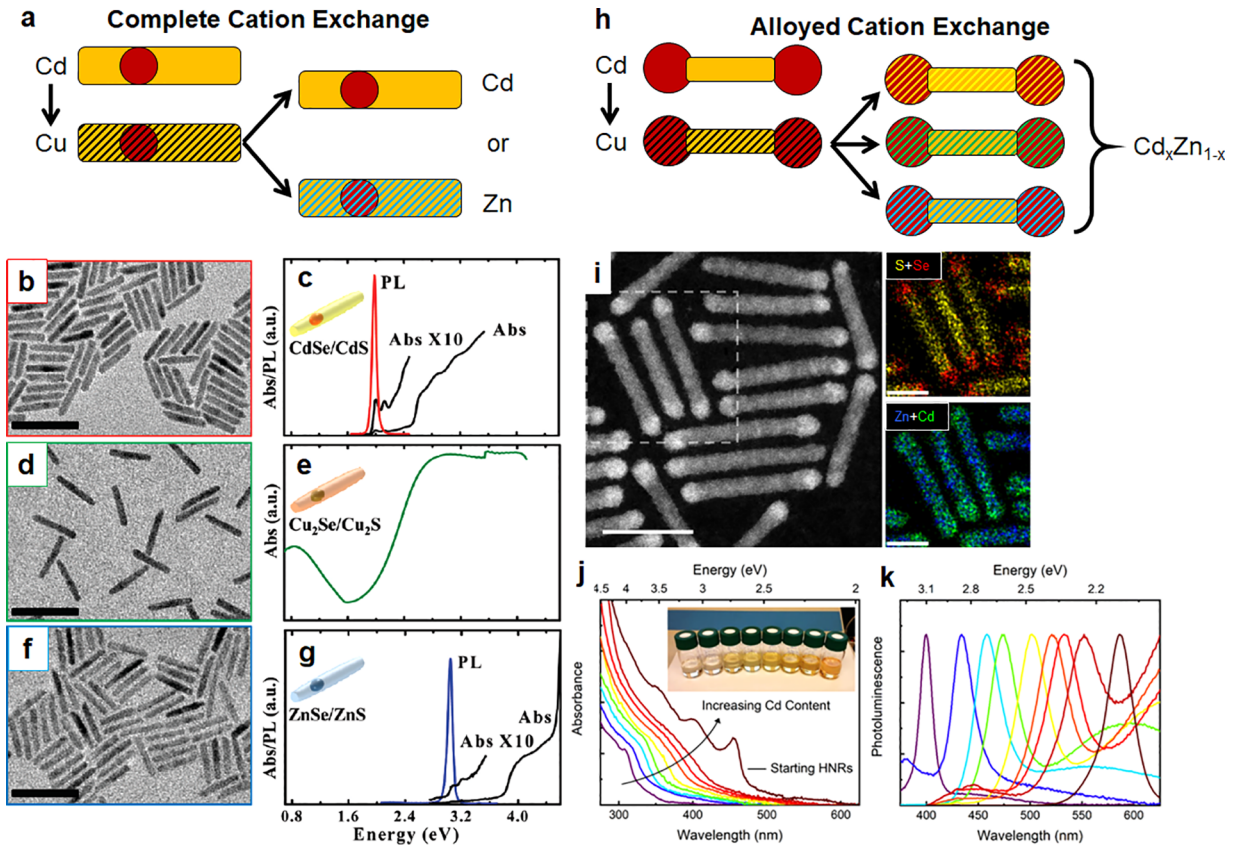

Figure 13. (a) Schematic of complete cation exchange from Cd to Cu, followed by a second complete exchange from Cu to either Cd or Zn. TEM and absorption and PL spectra of dot-in-rods for the original CdSe/CdS composition (b,c), Cu_2Se/Cu_2S (d,e), and ZnSe/ZnS (f,g).[67] (h) Schematic of cation exchange route to alloyed $Cd_xZn_{1-x}(S,Se)$ heterostructures, where the second cation exchange step uses a mixture of Cd and Zn together. (i) HAADF STEM micrograph and elemental EDX maps of (Cd,Zn)Se/(Cd,Zn)S/(Cd,Zn)Se barbell structures after alloyed cation exchange.[23] Absorption (j) and PL (k) spectra of alloyed barbell structures over a range of compositions between pure CdS/CdSe and pure ZnS/ZnSe.[23]

a cation-exchange-based approach to NRH synthesis. Ligands have different affinities for cations in solution, which provides the thermodynamic driving force for cation exchange and therefore becomes the primary consideration in the synthesis design. The affinity depends on the polarizability, following hard−soft acid−base theory: hard with hard (weakly polarizable), and soft with soft (strongly polarizable).[99] For example, the hard base methanol is commonly used to solvate Cd^{2+}, inducing exchange from Cd to Cu chalcogenide. The reverse process toward Cd or Zn chalcogenide is accomplished by extraction of Cu^{2+} using the soft base trioctylphosphine. Cation exchange is facilitated, often to completion, by this preferential affinity of organic ligands in solution to the initial cations in the lattice, along with the high diffusivity of the smaller cations and the small diffusion lengths required for nanoscale particles. Indeed, the energy barrier to cation exchange can be sufficiently low that it can be accomplished at a much lower temperature than heteroepitaxy (*e.g.*, at room temperature),[100] which can allow paths to otherwise difficult-to-access structures, both in terms of morphology and metastable phases.

There are also challenges cation exchange can bring to the synthesis of complex nanocrystal heterostructures. In some cases, cation exchange cannot be avoided under conditions intended for heteroepitaxy.[74] Metal deposition, rather than cation exchange, has also been observed under certain conditions.[101,102] With advances being made in understanding these phenomena, such potential problems can be either avoided or exploited in designing synthetic routes to a wide range of NRHs. As further discussed in the following section, even single-composition nanoparticles can be converted to novel multiphase heterostructures with carefully designed cation exchange approaches.

3. $Cu_{2-x}S$-BASED NANOROD HETEREOSTRUCTURES

The high cation mobility in superionic conductors and the short diffusion lengths needed in nanocrystals can be and has been exploited to expand the composition and morphologies of NRHs. Cation exchange using Cu-chalcogenides as intermediates for composition conversion was one such example discussed in the previous section, but there are many more ways superionic conductors can be used to design well-controlled synthetic pathways to NRHs of extraordinary complexity. In this section, we limit our discussion to NRHs starting with $Cu_{2-x}S$ nanorods or nanorods synthesized with the aid of $Cu_{2-x}S$ nanoparticles, but the concepts discussed should be applicable to other NRHs that are obtained through superionic-conductor-mediated synthesis. Among this class of materials, NRHs incorporating I−III−VI_2 compounds have been explored the most. However, due to the nascent nature of the field, even the reports of NRHs of I−III−VI_2 compounds are still relatively sparse. Nevertheless, these reports indicate that regioselectivity can be imparted through cation exchange. Furthermore, nanorods of I−III−VI_2 compounds, often

https://doi.org/10.1021/acs.chemrev.2c00410
Chem. Rev. XXXX, XXX, XXX−XXX

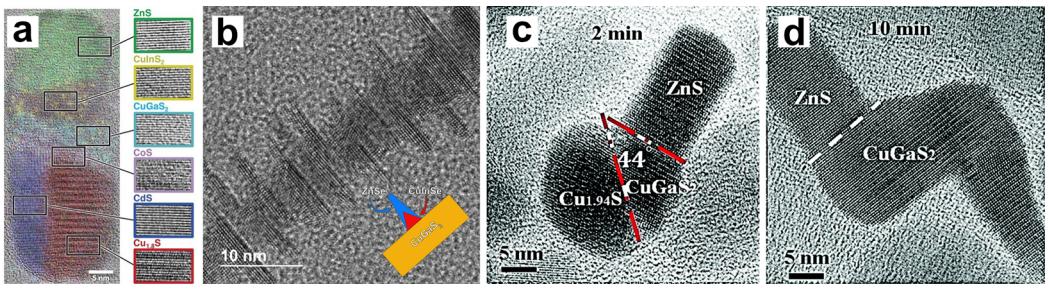

Figure 14. (a) "Exchanged" NRH formed by controlled cation exchange of an initial $Cu_{2-x}S$ nanorod. The exchange has been calibrated such that many different structures can be formed based on the desired final distribution of elements. The observed regioselective exchange is due to lattice strain between the base $Cu_{1.8}S$ nanorod, and the new phase resulting from cation exchange.[22] (b) $CuGaS_2/CuInSe_2/ZnSe$ nanorod exhibiting unusual branching structures grown by sequential heteroepitaxy.[103] (c) $Cu_{1.94}S/CuGaS_2/ZnS$ nanorod formed by cation exchange, showing the versatility of growth *via* superionic conductor. In this instance, it is unclear if the ZnS phase is grown *via* heteroepitaxy, or if it is the result of cation exchange, like the $CuGaS_2$ phase. (d) $CuGaS_2/ZnS$ structure with tapering $CuGaS_2$ end obtained by continued cation exchange of the $Cu_{1.94}S$ phase of the three-phase NRH in (c).[104] (c,d) Reproduced with permission from ref 104. Copyright 2016 Royal Society of Chemistry.

generated by a combination of cation exchange and epitaxial growth mediated by Cu-chalcogenides, can also be used as seeds for solution heteroepitaxy to achieve interesting NRHs.

We refer to heterostructures which are formed as a result of cation exchange with the starting nanorod maintaining its overall shape as "exchanged" NRHs, and heterostructures which are obtained by epitaxial growth onto existing nanorods (or epitaxial growth onto other shapes of nanocrystals leading to rods) as "epitaxial" NRHs. An example of an "exchanged" NRH is shown in Figure 14a and an example of an "epitaxial" NRH is shown in Figure 14b. In addition to these two types, there are NRHs arising from a combination of cation exchange and epitaxy, and examples of these structures are shown in Figure 14c,d. These structures are mainly the result of Cu-chalcogenide mediated growth of nanorods when such growths are stopped, intentionally or not, before complete cation exchange takes place, leading to *in situ* formation of NRHs. We first discuss $Cu_{2-x}S$-mediated nanorod growth and NRHs that form during such growths below before delving into exchanged and epitaxial NRHs.

3.1. Growth of I–III–VI_2 Nanorods *via* Superionic Conductors and *in Situ* Generated Nanorod Heterostructures

The I–III–VI_2 compounds represent a diverse family of inexpensive, environmentally benign semiconductors, with size-tunable emission spanning the width of the visible spectrum and expanding into the infrared (Figure 15). While Figure 15 does not contain all compounds that could be classified as I–III–VI_2, it contains the primary I–III–VI_2 compounds, which are typically investigated for photonic and electronic applications. In many cases, I–III–VI_2 materials exhibit growth mechanisms separate from II–VI compounds, which allow for unique approaches to create heterostructures. Although this additional pathway can complicate both the characterization and the synthetic design, with better understanding, it can also enable even finer synthetic control over highly complex structures.

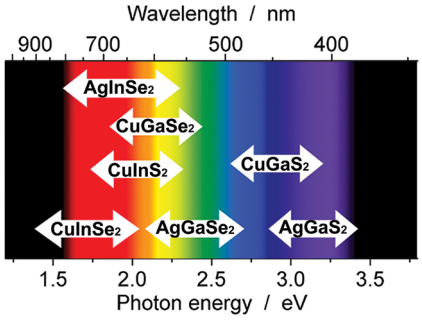

Figure 15. Calculated size-dependent band gap of selected I–III–VI_2 semiconductor nanocrystals. Reproduced with permission from ref 105. Copyright 2009 AIP.

Unlike conventional synthesis of II–VI nanorods, where homogeneous nucleation is followed by anisotropic homoepitaxy, many I–III–VI_2 nanorods are prepared through growth mediated by a superionic conducting phase. As a consequence of the high superionic conductivity of $Cu_{2-x}S$, the change from I_2–VI to I–III–VI_2 is facile in most circumstances, and the typical synthesis involves initial nucleation of I_2–VI particles in precursor solution, followed by a transition from binary to ternary or quaternary compound (*i.e.*, I_2–VI → I–III–VI_2 or I_2–VI → I–III–III–VI_2). The exact details of the growth of nanorods from these seeds is a matter of ongoing debate, but currently proposed mechanisms include solution-solid–solid (SSS),[106] diffusion-controlled growth (DCG),[107,108] catalyst-assisted growth,[109] and concurrent seed growth and cation exchange (CSC).[71] These mechanisms all identify cation exchange of the I_2–VI as critical to growth, but differ in the explanation given for anion lattice extension (if addressed).

Among these competing mechanisms, the CSC mechanism provides the most comprehensive explanation of the observed phenomena, addressing the issue of anion lattice extension while simultaneously explaining many morphological abnormalities (such as tapering and growth direction changes). CSC growth begins with the nucleation of a superionic I_2–VI seed, which almost immediately undergoes partial cation exchange, often leading to a Janus particle. As the reaction proceeds, epitaxial growth of the I_2–VI component continues, while cation exchange occurs concurrently. That is, epitaxial growth maintains the I_2–VI seed particle while cation exchange converts it to I–III–VI_2. Variations in the rates of these two reactions then determine many of the features observed in the resulting nanorod. The depletion of I_2–VI precursors causes a reduction in the epitaxial growth rate relative to the cation exchange rate and decreases the diameter of the superionic phase, leading to pronounced tapering. Eventually, the I_2–VI precursors are depleted entirely, and the whole nanorod is cation exchanged. The CSC growth mechanism is illustrated

https://doi.org/10.1021/acs.chemrev.2c00410
Chem. Rev. XXXX, XXX, XXX–XXX

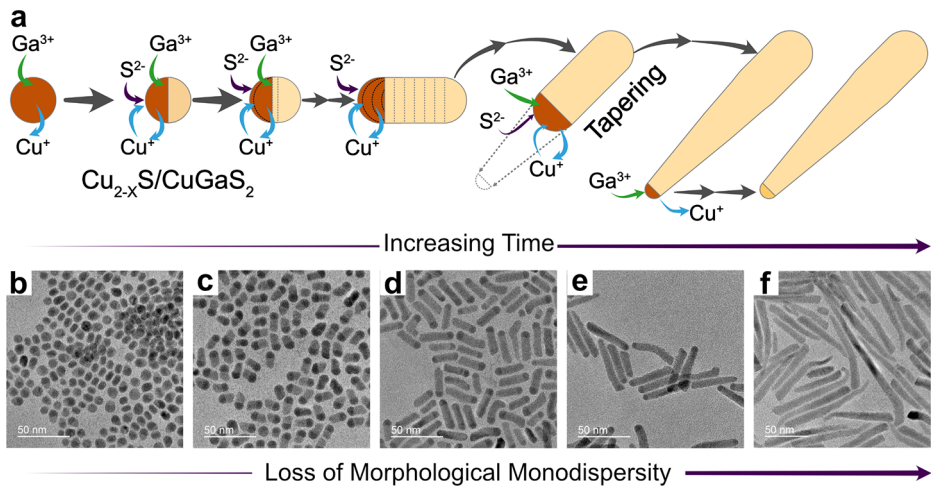

Figure 16. (a) Illustration of the concurrent seed growth and cation exchange (CSC) mechanism. Following the nucleation of a $Cu_{2-x}S$ particle, partial cation exchange occurs almost immediately. As the reaction proceeds, $Cu_{2-x}S$ epitaxy occurs concurrent with cation exchange of the superionic conductor phase. When the concentration of $Cu_{2-x}S$ precursor is depleted, cation exchange continues to occur, and a rod which is completely exchanged is formed. (b–f) TEM of $Cu_{2-x}S/CuGaS_2$ NRHs showing the different stages of NR growth. (a–f) Reproduced with permission from ref 71. Copyright 2021 Royal Society of Chemistry.

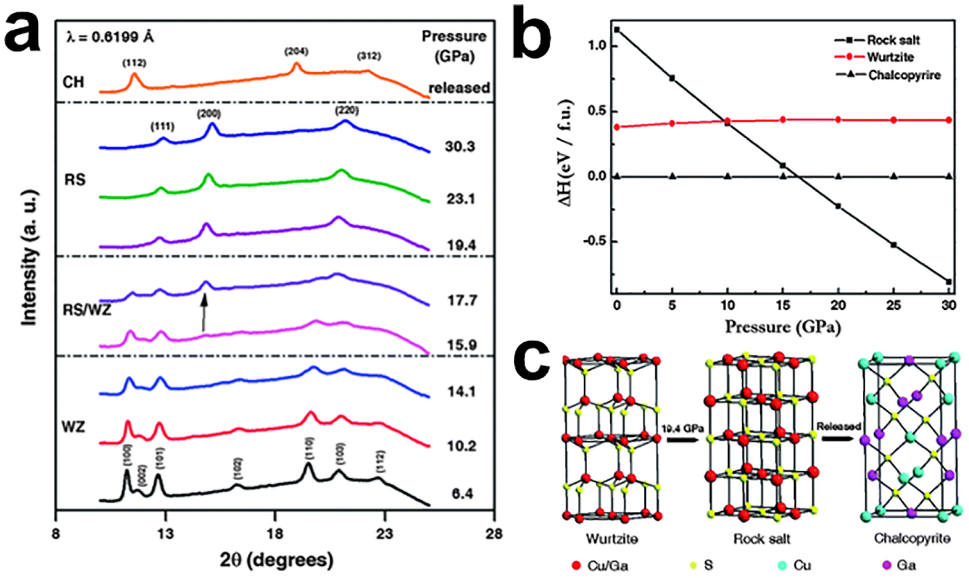

Figure 17. (a) XRD of $CuGaS_2$ NRs taken at different pressures showing the change in phase from wurtzite-like → rock salt → chalcopyrite, demonstrating that the wurtzite-like phase is metastable.[110] (b) Calculation of the change in energy per formula unit for the three different phases shown in (a) as a function of pressure, along with crystal models (c). The energy/pressure diagram suggests that the wurtzite-like phase should be inaccessible for NRs, however, it is basically the only phase observed for $CuGaS_2$ NRs. Reproduced with permission from ref 110. Copyright 2012 Royal Society of Chemistry.

schematically in Figure 16a, and TEM showing the different stages of CSC growth are shown in Figure 16b–f.

It is interesting and important to note that I–III–VI_2 nanorods grown *via* I_2–VI seeds exhibit the hexagonal wurtzite-like crystal structure despite this structure not being the preferred phase for I–III–VI_2 compounds under the given conditions. Prior work has shown that the chalcopyrite (zinc-blende-like) structure is energetically more favorable at ambient pressure than the wurtzite-like phase, as demonstrated by the pressure-induced phase transition from wurtzite-like to rock salt structure, which transforms to chalcopyrite structure upon release of pressure for $CuGaS_2$ (Figure 17a,b).[110] Yet the synthesis of $CuGaS_2$ nanorods from $Cu_{2-x}S$ seeds almost exclusively results in the wurtzite-like structure, likely due to the hexagonal anion template present in the $Cu_{2-x}S$ seed phase. $Cu_{2-x}S$ has many different phases, which are accessible with only minor changes in stoichiometry.[69] Because the cations in the lattice are highly mobile above a relatively low temperature and the growth is carried out above this critical temperature, the exact phase of $Cu_{2-x}S$ can be difficult to assign. However, this uncertainty is typically not an issue in nanorod growth, as most phases of $Cu_{2-x}S$ amount to a hexagonal lattice with varying degrees of distortion and disorder. The presence of the hexagonal lattice in the $Cu_{2-x}S$ phase coupled with the rigidity of the anion sublattice means that the cation exchange of $Cu_{2-x}S$ results in a hexagonal lattice as well.

https://doi.org/10.1021/acs.chemrev.2c00410
Chem. Rev. XXXX, XXX, XXX–XXX

During the Cu-chalcogenide mediated growth of I−III−VI_2 or II−VI nanorods, if the reaction is halted at any point before cation exchange is completed, a simple NRH with a I_2−VI tip will result. This approach has provided the largest range of NRH materials *via* Cu-chalcogenide-mediated one-pot synthesis to date. For such directly formed heterostuctures, the CSC mechanism seems to provide an explanation that is most widely consistent with reported observations. Figure 16b−d shows $Cu_{2-x}S$ tipped $CuGaS_2$ NRHs that are formed at different stages of $CuGaS_2$ nanorod growth.[71] Initially, the most abundant interface between $Cu_{2-x}S$ and $CuGaS_2$ is the $\{10\bar{1}2\}/\{10\bar{1}2\}$ junction, which minimizes lattice strain and the initial growth of $CuGaS_2$ occurs along ⟨10−12⟩ direction, which is the closest direction perpendicular to this interface that gives rise to low-index terminating side facets. Here, crystallographic indices referring to the hexagonal anion sublattice are used for clarity and simplicity. Eventually, the overall surface energy favors the ⟨0001⟩ growth direction and leads to the observed kinks as the rod length increases until they become dominating features (along with tapering) in the final complete single-phase $CuGaS_2$. The epitaxial growth of $Cu_{2-x}S$ tip concurrent with cation exchange at the interface, that is, the CSC mechanism, accounts for the tapering as described earlier and can also lead to a "fluid" interface due to liquid-like cations on the $Cu_{2-x}S$ side, where cation exchange is occurring that can accommodate the growth direction change observed.

The structure shown in Figure 14c is another example of a NRH synthesized by interrupting the growth and cation exchange of the I_2−VI component to a nanorod of a different composition.[104] Despite having three different components that appear to lead to a complex structure and therefore the authors' description of its possible growth mechanism lacking some key details, it too may be explained within the CSC growth mechanism. In this synthesis, $Cu_{2-x}S/ZnS$ matchstick structures are first synthesized and cleaned. These matchstick heterostructures are then reacted with $Ga(acac)_3$ and dodecanethiol as Ga and S precursors, respectively, resulting in the three-component structure shown in Figure 14c. When the reaction is carried out to completion, a tapering biphasic $ZnS/CuGaS_2$ NRH (shown in Figure 14d) is obtained. In the three-phase intermediate, the $Cu_{2-x}S/CuGaS_2$ interface forms a 44° angle with the $CuGaS_2/ZnS$ interface. That is, given the $\{0001\}/\{0001\}$ junction between $Cu_{2-x}S$ and ZnS, the $Cu_{2-x}S/CuGaS_2$ interface should be the $\{10\bar{1}2\}/\{10\bar{1}2\}$ junction. This is the same interface seen in the previous example, where, as cation exchange initiates, the lowest strain interface dominates. The change in the growth direction and the tapering exhibited in this system can also be explained by the overall surface energy reduction, altering the growth direction and increasing cation exchange rate relative to $Cu_{2-x}S$ epitaxial growth rate decreasing $Cu_{2-x}S$ size leading to tapering, the main premises of CSC mechanism.

NRHs prepared by methods similar to the $CuGaS_2$ nanorod growth, that is, interrupting a combination of cation exchange and epitaxial growth, have been reported most frequently among $Cu_{2-x}S$-based heterostructures and are summarized in Table 1. We note that this table represents a collection of NRHs synthesized *starting from Cu-chalcogenide seeds*, separately synthesized or generated *in situ*. Although multiple different stoichiometries for Cu-chalcogenide seeds are reported, we have classified and grouped them all as $Cu_{2-x}S$ because assigning the "true" stoichiometry of $Cu_{2-x}S$, in cases of $x \approx 0$, is challenging. Furthermore, the reported morphologies of these structures vary and have been coined many different terms. Because many of these structures appear to be nanorods that contain different degrees of tapering and bends, we simply refer to these particles as "nanorods" unless a particular dimension is sufficiently different to merit a change in terminology (*e.g.*, nanowires and nanoribbons). Finally, we note that while cation exchange being a part of the growth mechanism is fairly well accepted for all of these structures, whether the further growth of the second phase after the initial cation exchange is direct homoepitaxy of the new phase or epitaxy of $Cu_{2-x}S$ followed by cation exchange, remains under discussion. However, in cases where partially exchanged $Cu_{2-x}S$ remains until the end, where it undergoes final complete cation exchange, we argue that the CSC mechanism is the only viable explanation among those proposed. Otherwise, it would require cation exchange to be favorable only at the extremes of precursor concentrations (*i.e.*, at the beginning and the end of the reaction) but not at any intermediate concentrations during the growth, which is highly unlikely.

Table 1. Collection of Heterostructures Achieved during $Cu_{2-x}S$-Mediated Growth That Includes Partial Cation Exchange

materials	structure	ref
$Cu_{2-x}S/CuGaS_2$	nanorod, nanotadpole	71,108
$Cu_{2-x}S/ZnS$	nanorod	111,112
$Cu_{2-x}S/CuInS_2$	nanorod, nanoribbon	112−118
$Cu_{2-x}S/CuGaS_xSe_{2-x}$	nanoribbons	119
$Cu_{2-x}S/MnS$	nanorod	120
$Cu_{2-x}S/CuInZnS_2$	nanorod	112
$Cu_{2-x}S/Cu_2ZnSnS_4$	nanoleaf	121
$Cu_{2-x}S/Zn_xCd_{1-x}S$	nanorod	122
$Cu_{2-x}S/In_2S_3$	nanorod	109
$Cu_{2-x}S/CuIn_xGa_{1-x}S_2$	nanoribbon	118

3.2. Exchanged Nanorod Heterostructures

In this section, we focus on NRHs that have been achieved *via* partial cation exchange starting from $Cu_{2-x}S$ nanorods, which retain their initial shape and with nominally no volume increase due to other complicating parallel reactions such as epitaxy. There have also been several reports of NRHs synthesized *via* cation exchange from CdS/Se/Te or other materials, but a full treatment of these structures is beyond the scope of this review. For such materials, we refer the readers to other reviews on cation exchange of nanostructures.[96]

Table 2 lists exchanged NRHs derived from $Cu_{2-x}S$ nanorods. While the list is limited, indicating much need for

Table 2. Collection of Heterostructures Formed by Cation Exchange of Pre-Existing $Cu_{2-x}S$ NRs[a]

materials	structure	ref
$Cu_{2-x}S/ZnS$	nanorod	22,40,123,124
$Cu_{2-x}S/CdS$	nanorod	22,123,124
$Cu_{2-x}S/CuGaS_2$	nanorod	22,42
$Cu_{2-x}S/CuInS_2$	nanorod	22,42
$Cu_{2-x}S/CoS$	nanorod	22
$Cu_{2-x}S/Cu_{2-x}Te$*	nanorod	125

[a]*This structure is formed *via anion* exchange, but the principles discussed in this section still apply.

https://doi.org/10.1021/acs.chemrev.2c00410
Chem. Rev. XXXX, XXX, XXX−XXX

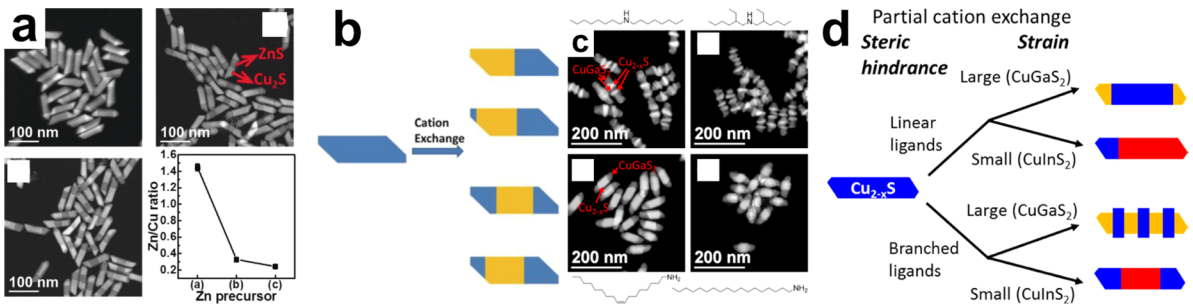

Figure 18. (a) TEM of Cu_2S/ZnS NRHs showing regioselective cation exchange dependent on Zn precursor concentration.[40] (b) Scheme demonstrating the growth of Cu_2S/ZnS NRHs depending on the initial cation exchange, and the resulting structures.[40] (c) TEM of $Cu_{2-x}S$/$CuGaS_2$ NRHs demonstrating the effect of different ligands on the regioselectivity of the cation exchange procedure.[42] (d) Scheme summarizing the effect of steric hindrance and strain on the regioselectivity of cation exchange within $Cu_{2-x}S$ NRHs.[42] Reproduced with permission from ref 42. Copyright 2017 American Chemical Society.

further studies in this area, there are very interesting structures and some of the very same principles discussed in the II−VI epitaxial NRHs section earlier can be applied to explain and control these structures. In particular, we highlight the effects of ligand steric hindrance and lattice strain.

3.2.1. Surface Ligand and Precursor Steric Hindrance. Similar to the difference in ligand passivation on different terminating facets of II−VI nanorods leading to regioselective nucleation and growth in heteroepitaxy discussed earlier, cation exchange to achieve biphasic NRHs has been shown to be strongly influenced by the choice of ligands. Figure 18c shows $Cu_{2-x}S$ nanorods with different ligand passivation that have undergone partial cation exchange with Ga ions. Linear chain primary amines as surface passivating ligands (*e.g.*, oleylamine or octadecylamine) lead to cation exchange that initiates at the tips. Bulkier secondary amines (*e.g.*, dioctylamine or bis(2-ethylhexyl)amine) show distinctly different results where the cation exchange occurs both at the tips and at the sides of the nanorods. The interaction between linear primary amines causes a large steric barrier for the cation complex in solution to reach the surface of the nanorod to initiate cation exchange. The tips, where the surface curvature causes the ligand tails to be spread further apart, allow easier delivery of the cations to the surface and imparts the regioselective tip preference. Bulkier ligands, with less van der Waals interaction between them on the surface of the nanorod, reduce this steric barrier for diffusion to the surface especially on the side facets, allowing cation exchange to initiate both on the sides and tips. The interesting superlattice-like structure, where the nanorod has alternating phases that are nearly evenly spaced, is a consequence of multiple regions being nucleated due to lattice strain and is discussed later.

Analogous to steric effects of surface-bound ligands, the bulkiness of precursors for the incoming cation can also have a significant impact on cation exchange. When partial cation exchange is carried out on $Cu_{2-x}S$ nanorods using different Zn ion precursors, the least-bulky precursor allows the largest degree of cation exchange to occur with all other reaction conditions being equal (Figure 18a). The smallest Zn-acetate leaves the majority of the NRHs converted to ZnS often with only one small $Cu_{2-x}S$ domain on one tip, whereas the bulkier Zn-stearate and Zn-acetylacetonate convert only a small region often in the middle of the nanorod into ZnS. In the case of the smallest precursor, the steric effect imposed by the surface-bound ligands dominate, leading to the enhanced penetration of Zn ions through the less-dense surface ligand layer at the tips. Bulky ligands, on the other hand, introduce significant steric hindrance themselves that can effectively overrides this tip-preferred steric effect of the surface-bound ligands. In this scenario, the tip preference is lost and a much larger portion of the surface area of the nanorod being on sides than at the tips leads to cation exchange being more frequently observed somewhere in the middle of the nanorod. Such differences in the location of the partial cation exchange, and therefore of remaining $Cu_{2-x}S$ domains, can have important consequences. In particular, if there is either subsequent or concurrent epitaxial growth occurring, as the majority of $Cu_{2-x}S$-mediated nanorod growth cases discussed in the previous section do, the resulting NRHs can have significantly different morphologies, including different diameter modulation, length, and degree of tapering.

It is worthwhile noting that the ligand choice, whether it is to impart regioselectivity through anisotropic surface diffusion barrier or to vary overall rate through precursor bulkiness, needs to be carefully considered because the difference in the ligand affinity to cations in the lattice *vs* those in solution will determine whether or not cation exchange will occur in the first place. This consideration can place a significant limitation on the choice of ligands that can be used to design selective cation exchange reactions. One approach to circumvent this problem has been to use two distinct ligands, one to passivate the surface and the other to drive the cation exchange reaction.[42]

3.2.2. Exploiting Lattice Strain. While the presence of lattice strain between disparate materials is nearly inevitable and can lead to undesirable effects such as defect formation, it can also provide a unique opportunity in the synthesis of colloidal NRHs. In the epitaxial growth of II−VI NRHs discussed earlier, lattice strain has been shown to be an important determining factor in the morphology of the shell grown on the seed nanorod. In exchanged NRHs, lattice strain can play a critical role in the regioselectivity, exchanged domain number, size, and interface orientation of cation exchange.

A striking example of lattice strain effect on exchanged NRHs is shown in Figure 19a−e, where partial cation exchange of $Cu_{2-x}S$ nanorods using Ga ions leads to superlattice-like NRHs with alternating $CuGaS_2$ and $Cu_{2-x}S$ domains, whereas using In ions results in singly segmented $Cu_{2-x}S$/$CuInS_2$/$Cu_{2-x}S$ rod−rod−rod NRHs. The expected lattice mismatch of $CuGaS_2$ with djurleite $Cu_{2-x}S$ is 5.0% in the radial direction and 7.4% in the axial direction, while that with $CuInS_2$ is

https://doi.org/10.1021/acs.chemrev.2c00410
Chem. Rev. XXXX, XXX, XXX−XXX

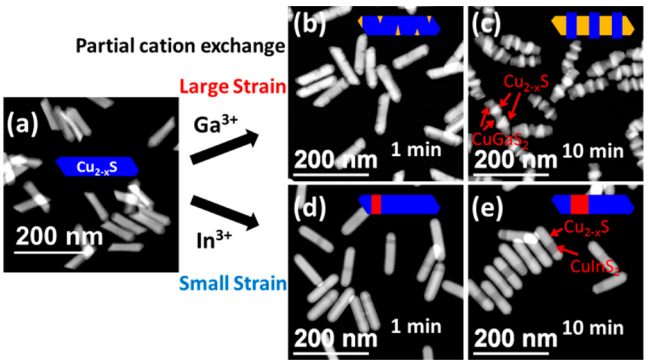

Figure 19. (a) Starting $Cu_{2-x}S$ NRs prior to cation exchange. (b,c) $Cu_{2-x}S/CuGaS_2$ NRHs at 1 and 10 min of exchange showing the formation of a superlattice-like structure. (d,e) $Cu_{2-x}S/CuInS_2$ NRHs at 1 and 10 min of exchange showing the growth of a rod−rod−rod NRH.[42]

expected to be only 0.7% in the radial direction, and 4.3% in the axial direction. As such, the $Cu_{2-x}S/CuGaS_2$ case can be considered to be relatively highly strained, while the $Cu_{2-x}S/CuInS_2$ case is only moderately strained. The large lattice strain limits the size of the $CuGaS_2$ domains during cation exchange, leading to the superlattice-like structure. Previously, a similar effect has also been reported with partial cation exchange of CdS nanorods with Ag ions.[126] In this system, *ab initio* simulation of the superlattice structure has indicated that the strain present between the CdS and Ag_2S forms a repulsive field which prevents further ripening of the Ag_2S domains, resulting in the metastable superlattice structure. We note that for the CdS/Ag_2S case, the initial Ag_2S nucleation appears as protrusions outside the CdS nanorods, whereas for the $Cu_{2-x}S/CuGaS_2$ case, the initial $CuGaS_2$ nucleation occurs *via* infiltration of Ga ions into $Cu_{2-x}S$ nanorods (Figure 19b), as expected of the cation exchange process.

Lattice mismatch and the resulting strain can provide further delicate control over the cation exchange process, providing accessible routes to highly complex NRHs. By using $Cu_{2-x}S$ nanorods as the base material, multiphase NRHs with different interface angles have been demonstrated as shown in Figure 20. Here, the minimization of lattice strain has been identified as the driving force for the observed interface angles in NRHs created through partial cation exchange of $Cu_{2-x}S$ nanorods.[127] Furthermore, by changing the order in which the desired phases are introduced in a multistep cation exchange process, regioselectivity can be imparted. For example, where and what interfaces form with CdS when $Cu_{2-x}S$ nanorods undergo partial cation exchange with Cd ions will depend on whether or not partial cation exchange with Zn ions has been carried out prior to Cd−cation exchange. The heterointerface between $Cu_{2-x}S$ and ZnS has minimal strain when the *a*-axis of the ZnS component is aligned with the *a*-axis of the $Cu_{2-x}S$ component. That is, the {0001}/{0001} junction (again, using hexagonal close packing crystallographic indexing for simplicity) minimizes strain at the $Cu_{2-x}S/ZnS$ interface. Conversely, the strain is minimized with an interface involving {10$\bar{1}$0} planes between $Cu_{2-x}S$ and CdS. When partial cation exchange using Cd ions is carried out prior to cation exchange with Zn ions, CdS grows from one tip and forms a diagonal interface as

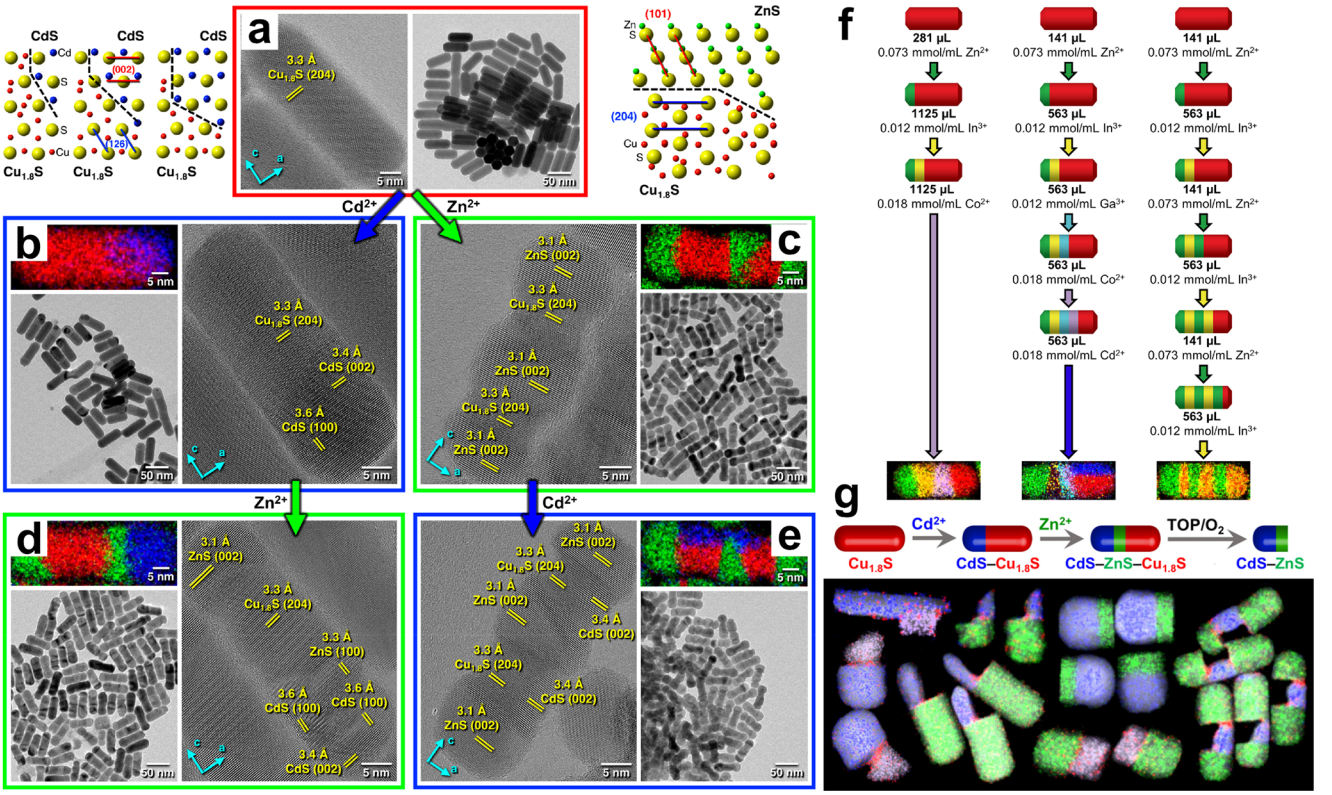

Figure 20. (a) Initial $Cu_{2-x}S$ NRs, along with the crystal structures, and expected interfaces between $Cu_{2-x}S$ and CdS or ZnS. (b−e) The results of cation exchange of $Cu_{2-x}S$ NRs, which results in distinct structures based on the order of exchange.[123] (f) Scheme showing the reaction conditions for regioselective cation exchange which makes up the basis for the complex structure shown in Figure 14a.[22] (g) Continuation of the work shown in (a−e), where the $Cu_{1.8}S$ component can be selectively etched after cation exchange to yield unique morphologies.[124]

https://doi.org/10.1021/acs.chemrev.2c00410
Chem. Rev. XXXX, XXX, XXX−XXX

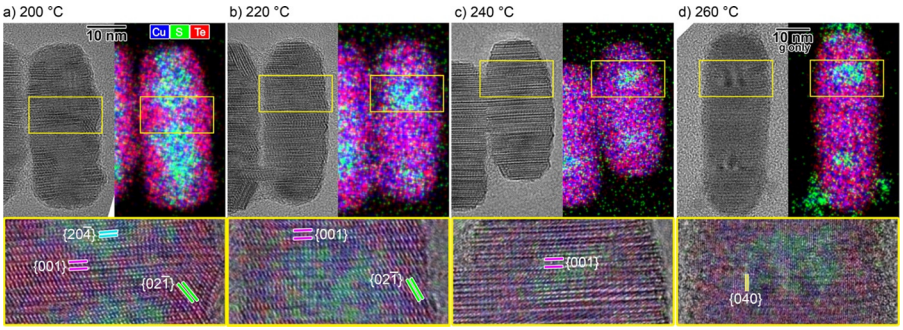

Figure 21. (a–d) Anion exchange of $Cu_{2-x}S$ NRs to $Cu_{2-x}S/Cu_{2-x}Te$ as a function of temperature. At the highest temperature, the NRs are almost completely exchanged to $Cu_{2-x}Te$.[125]

shown in Figure 20b. However, when ZnS is first formed prior to Cd–cation exchange, Cd ion infiltration occurs from the side facets, leading to interface with $Cu_{2-x}S$ that is parallel to the rod's long axis (Figure 20e). A similar strategy using a wide variety of compositions to achieve a "megalibrary" of multiphase NRHs has also been demonstrated using up to six different phases in a single nanorod (Figure 14a and Figure 20f).[22] Even further complexity in NRHs can be achieved when this strategy for multiphase NRHs is coupled with selective etching as demonstrated in Figure 20g. Selective etching of the remaining $Cu_{2-x}S$ domain allows for the construction of complex NRHs with unique morphologies.[124] Selective etching of spherical $Cu_{2-x}S$ nanocrystals that had been partially cation exchanged to form ZnS at the opposite poles have been shown to lead to nanorod-like heterostructures earlier.[128]

Because the rods studied in the multistep cation exchange approach described above are relatively large (~20 nm in diameter), the effects of strain are expected to be prominent. It would be interesting to explore how this strain-induced preference in interfaces evolve with decreasing diameter down to the regime of strong quantum confinement.

We note that anion exchange is a much more difficult process[129] that has rarely been reported for $Cu_{2-x}S$-based materials but could open up exciting directions in NRHs and beyond. In addition to the anions being "locked" in a more rigid sublattice than the cations, anion exchange can often lead to the Kirkendall effect,[130] easily leading to the loss of morphology of the initial nanorod. A recent work showed that these difficulties can be overcome and demonstrated the possibility of controlled S-to-Te anion exchange of $Cu_{2-x}S$ rods as shown in Figure 21a–d.[125] Initially, the anion exchange happens at the surface, resulting in a core/shell NRH. Eventually, exchange of the anion proceeds to a point where a double-core structure is formed. Finally, the rod is completely exchanged to Cu_2Te. Here, the facile anion exchange is attributed to the presence of stacking faults within the host $Cu_{2-x}S$ nanorods, which act as channels for diffusion and avoids void formation expected in the Kirkendall effect, meaning that the morphology of the original NR is largely retained. The ability to perform topotactic selective anion exchange of $Cu_{2-x}S$ seeds considerably expands the parameter space of accessible for heterostructure synthesis and the available energy band alignments for the resulting NRHs.

3.3. Epitaxial Nanorod Heterostructures

As defined previously, the epitaxial heterostructures considered here are those in which a secondary component is grown on a pre-existing substrate or seed nanocrystal *via* direct epitaxy. Heterostructures achieved through this growth mechanism is considerably rare when starting with $Cu_{2-x}S$ nanocrystal as the "substrate." The lack of such structures is, at least in part, due to the high cation mobility of $Cu_{2-x}S$ making cation exchange likely at the elevated temperatures necessary for most epitaxial growth schemes. Hence, most NRHs in this class start from materials derived from $Cu_{2-x}S$ nanocrystals, namely I–III–VI_2 compounds, as the substrate. A summary of such epitaxially grown NRHs based on $Cu_{2-x}S$ is shown in Table 3. We note

Table 3. List of $Cu_{2-x}S$-Based Epitaxial NRHs

substrate/epilayer	structure	ref
$CuInS_2$/ZnS	dot-in-rod	133
$Cu_{2-x}S$/ZnS	rod–rod	134
$CuGaS_2$/($CuInS_2$,$CuInSe_2$) + (ZnS,ZnSe)	dots- or spikes-on-rod	103
($CuInS_2$,$CuInZnS_2$)/CdS	dot-in-rod	135
($CuGaS_2$,$CuInS_2$)/(CdS,ZnS)	plates-on-rod	136

that there are additional reports of similar NRHs (*e.g.*, refs 131 and 132), but they do not explicitly state or observe $Cu_{2-x}S$ intermediates during the growth of the seed nanocrystals.

In the dot-in-rod structures, the main advantage of using $Cu_{2-x}S$ as an intermediate to obtain I–III–VI_2 dots appears to be in achieving wurtzite-like structure of the seed nanocrystals.[133,135] The energetically favored chalcopyrite structure will hinder rod-shaped shell growth similar to the zinc blende structure, whereas the wurtzite-like structure will facilitate such a growth using essentially the same reaction conditions as those established for II–VI dot-in-rods. For the remaining three NRH types, we briefly highlight the effects of lattice strain (rod–rod and spikes-on-rod) and the reactivity of precursors (plates-on-rod) on their growth mechanisms.

3.3.1. Role of Lattice Strain. In the rare case of epitaxial growth starting from $Cu_{2-x}S$ seed nanocrystals, lattice strain can have a similar effect as that seen in the cation exchange of $Cu_{2-x}S$ nanorods. Xia *et al.* recently reported the synthesis of $Cu_{2-x}S$/ZnS structures *via* seeded growth.[134] In their synthesis, $Cu_{2-x}S$ nanocrystals were injected into a hot Zn(oleate)$_2$ stock solution, followed by an injection of TOPO/S, which resulted in a two-component $Cu_{2-x}S$/ZnS NRH (Figure 22c). The growth of this NRH is proposed to proceed *via* a seeded growth mechanism, wherein the $Cu_{2-x}S$ nanocrystals act as the substrate, and ZnS monomers add epitaxially (Figure 22d). The epitaxial growth of ZnS in this instance appears to be due to the combination of low lattice mismatch with the $Cu_{2-x}S$ substrate (~2.1%), and ligand coverage of the $Cu_{2-x}S$ particle which favors growth on the {0001} facet. The authors have

https://doi.org/10.1021/acs.chemrev.2c00410
Chem. Rev. XXXX, XXX, XXX–XXX

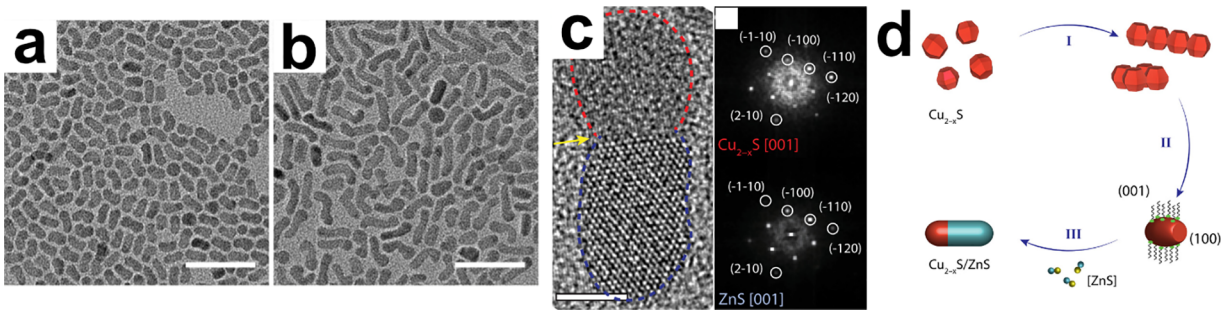

Figure 22. (a,b) TEM of $Cu_{2-x}S/ZnS$ NRHs synthesized by hot injection of $Cu_{2-x}S$ seeds into Zn-oleate solution. (b) has a higher concentration of Zn precursor than (a). Scale bar in both images is 50 nm (c) HRTEM of $Cu_{2-x}S/ZnS$ NRHs showing the difference in lattice structure *via* fast Fourier transform (FFT) of the HRTEM image. Scale bar is 5 nm. (d) Schematic depicting the proposed growth mechanism of these NRHs. In this proposed mechanism, the growth of $Cu_{2-x}S$ seeds occurs *via* coalescence of smaller $Cu_{2-x}S$ particles. These coalesced particles are then well-ligated in the growth environment. Then, when ZnS precursor is added, the growth of ZnS occurs epitaxially, due in part to the small lattice mismatch between ZnS and $Cu_{2-x}S$.[134]

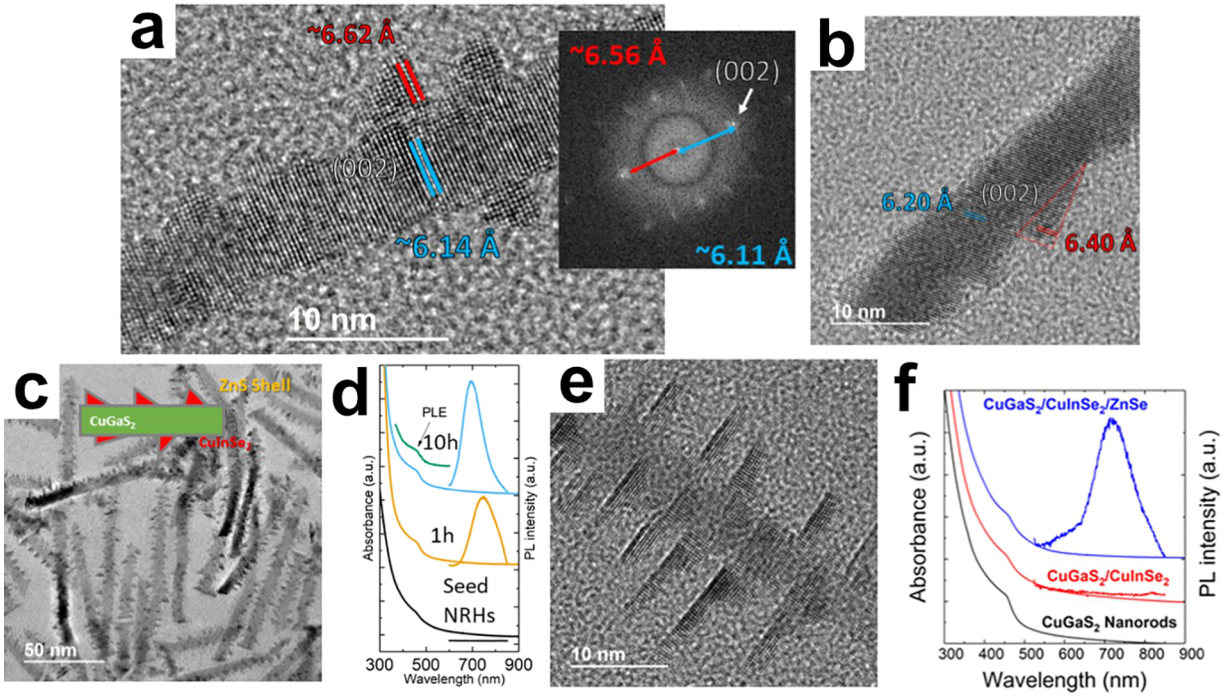

Figure 23. (a) TEM of $CuGaS_2/CuInSe_2$ colloidal NRH with annotated difference in lattice parameter between the body of the rod and the epitaxial growth. (b) TEM of $CuGaS_2/CuInS_2$ colloidal NRH with annotated difference in lattice parameter between the body of the rod and the epitaxial growth.[103] The difference in lattice parameter between the $CuGaS_2$ substrate and the epitaxial component is responsible for the difference in shape observed between the epitaxial components. The shape of the protrusions suggests that epitaxial growth in this instance proceeds *via* Stranski–Krastanov or Volmer–Weber growth. (c,d) TEM and UV–vis/PL spectra of $CuGaS_2/CuInSe_2/ZnS$ NRHs. (e,f) TEM and UV–vis/PL spectra of $CuGaS_2/CuInSe_2/ZnSe$ NRHs.

also carried out *in situ* heating TEM studies and observed that the $Cu_{2-x}S$ nanocrystals coalesce to form larger particles. While the *in situ* heating measurements were carried out in vacuum, which is very different than in solution with various reagents where the actual reaction is carried out, they do verify that $Cu_{2-x}S$ nanocrystals are highly dynamic at temperatures commonly employed in nanorod synthesis and can contribute to the anisotropic growth of $Cu_{2-x}S$. *Ex situ* TEM of aliquots taken at early stages of the reaction show increased $Cu_{2-x}S$ nanocrystal size, often elongated into rod shape, followed by ZnS growth. It is interesting to note that a mechanism similar to the CSC growth (where $Cu_{2-x}S$ grows as rods and concurrent cation exchange converts part of that rod into ZnS) could be at play here. The extension of the $Cu_{2-x}S$ lattice would then be through coalescence or ripening of $Cu_{2-x}S$ particles and this mechanism would also explain the frequently observed bends or kinks in the resulting NRHs (Figure 22a,b). Further studies verifying heteroepitaxy at the ZnS tip or concurrent cation exchange and therefore ZnS growth occurring at the $Cu_{2-x}S/ZnS$ interface would be highly insightful. Nevertheless, the resulting interface of $Cu_{2-x}S/ZnS$ structures appears to be consistent with preference for the low-lattice-mismatch junction. Furthermore, $Cu_{2-x}S/ZnS$ NRHs provide an additional advantage for heterostructure design through $Cu_{2-x}S$-mediated synthesis. Replacing Zn ions in these NRHs *via* cation exchange results in single-phase $Cu_{2-x}S$ NRs with considerably smaller dimensions than is possible by currently available direct synthesis approaches,

https://doi.org/10.1021/acs.chemrev.2c00410
Chem. Rev. XXXX, XXX, XXX–XXX

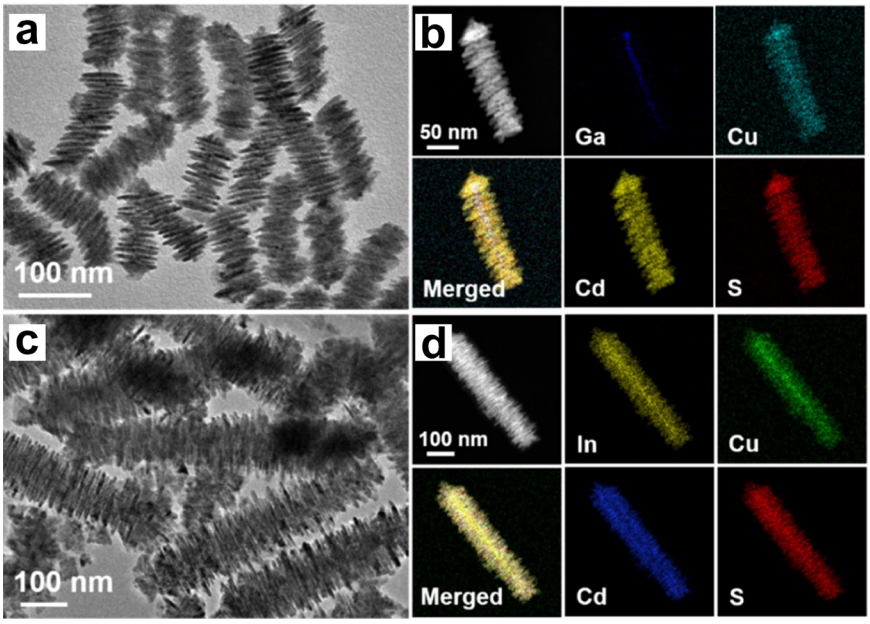

Figure 24. (a,b) TEM, STEM, and EDS of $CuGaS_2$/CdS NRHs. (c,d) TEM, STEM, and EDS of $CuInS_2$/CdS NRHs.[136]

expanding the size range where heterostructures based on $Cu_{2-x}S$ nanorods can be explored.

Nanorods of I−III−VI_2, in particular $CuGaS_2$, have also been synthesized through $Cu_{2-x}S$-mediated approaches with diameter <10 nm and have been utilized as seeds or substrates for subsequent heteroepitaxial growth. Figure 23a shows $CuInSe_2$ grown epitaxially on a $CuGaS_2$ nanorod substrate.[103] The $CuGaS_2$ nanorods in this case were grown from $Cu_{2-x}S$ seeds *via* CSC growth until the $Cu_{2-x}S$ portion was completely eliminated. Measurement of the lattice parameters of the final NRHs shows that the individual components (*e.g.*, $CuGaS_2$, $CuInSe_2$) are well segregated, *i.e.*, not alloyed, and the growth forms radially protruding islands. Within the same work, $CuInS_2$ was also grown on $CuGaS_2$ nanorods, as shown in Figure 23b. Again, a clear difference in the lattice parameter was observed, but the size and slope of the radial protrusions is significantly reduced compared to the $CuInSe_2$ case. When there is a large mismatch in lattice parameter, Stranski−Krastanov or Volmer−Weber growth may result. Due to instrument limitations, it has not been possible to determine if a wetting layer has grown around the entirety of the nanorod before the growth of the protrusions. However, it is clear that the extent of the radial growth of the protrusions on the $CuGaS_2$ substrate is related to the degree of lattice mismatch. Therefore, smaller lattice mismatch allows $CuInS_2$ particles to grow with a larger base interfaced with the substrate $CuGaS_2$ than $CuInSe_2$ particles with the larger lattice mismatch. This same work has also achieved the growth of a ZnS or ZnSe shell on the $CuGaS_2$/$CuInE_2$ (E = S, Se) NRHs (Figure 23c,d), demonstrating that multicomponent epitaxy is accessible for the I−III−VI_2 system. Moreover, heteroepitaxy of ZnSe on $CuInSe_2$ led to extended brush-like structures (Figure 23e,f). This brush-like morphology has also recently been demonstrated for several other compositions (Figure 24).[136]

3.3.2. Role of Precursor Reactivity. Recently, Li *et al.* have demonstrated heteroepitaxy of CdS or ZnS on CdSe, $CuGaS_2$, $CuInS_2$, CdS, and ZnS nanorods.[136] Structures starting from $CuGaS_2$ and $CuInS_2$ nanorods grown *via* $Cu_{2-x}S$-mediated approach, relevant ones for our discussion, are shown in Figure 24. The high concentration of ammonium thiocyanate (NH_4SCN) as a sulfur source has been identified as a critical factor in the growth of these NRHs. Thiocyanate is a known ligand for nanocrystals that can replace native ligands on the surface[137] and therefore has been suggested to easily adsorb on the surface of the seed nanorods. Furthermore, when CdS was synthesized using NH_4SCN as the sulfur source in the absence of the seed nanorods, nanoplatelets were obtained.[136] Hence, NH_4SCN appears to be a precursor that can efficiently deliver S to all surface-terminating facets of the seed nanorod and promote anisotropic growth along directions perpendicular to the seed rod's principal axis. However, when the concentration of NH_4SCN is reduced by a factor of 2, $CuGaS_2$/CdS core/shell NRHs resulted. This indicates that high reactant concentration, which increases the reaction rate, also plays a critical role in anisotropic growth. Hence, the same plates-on-rod structure achieved across several different rod compositions (CdSe, CdS, ZnS, $CuGaS_2$, and $CuInS_2$) and plate compositions (CdS and ZnS) seems to be independent of lattice strain, presumably due to the fast growth rate which indicates that this synthesis is dominated by reaction kinetics. This kinetic approach may lead to complications when size-specific or regioselective growth is desired but represents an interesting approach for certain applications where structures with high surface area are beneficial.

4. SELECTED APPLICATIONS OF NANOROD HETEROSTRUCTURES

In addition to the well-known size-tunable optical properties of colloidal quantum dots, NRHs can impart multiple dimensions to tailoring materials' properties. Reduced symmetry can bring about optical anisotropy, polarized light emission,[50,138,139] and lifting of energy state degeneracy.[31,140] It also leads to directionality useful for charge separation and extraction. Diameter modulation along the length of nanorods, which may be achieved through ligand choice as in the dual-diameter dot-in-rods,[32] through tapering effect in $Cu_{2-x}S$-mediate growth,[71] or through graded alloying,[141] can provide added advantages in directing charges or excitons. Each distinct phase within the

https://doi.org/10.1021/acs.chemrev.2c00410
Chem. Rev. XXXX, XXX, XXX−XXX

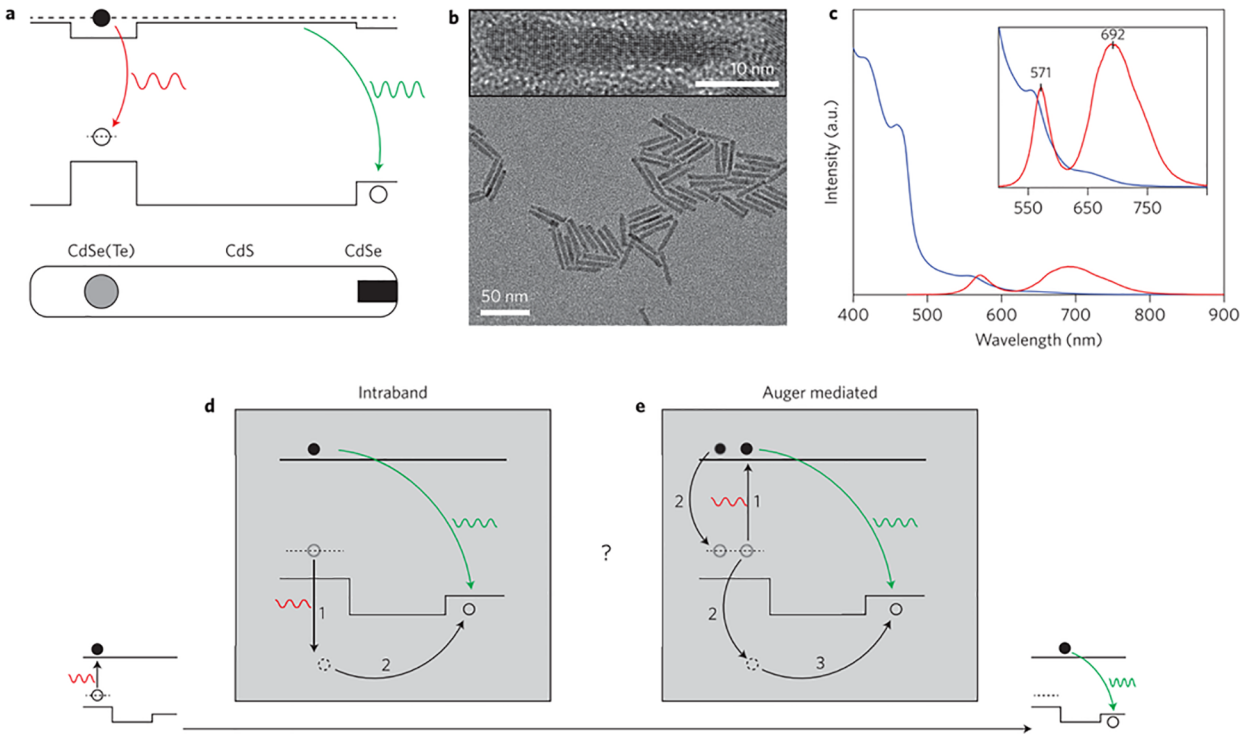

Figure 25. An overview of Cd(Se,Te)/CdS/CdSe barbell-like nanorod heterostructures for luminescence upconversion. (a) Schematic of dual emitting NRH. (b) High (top) and low (bottom) TEM micrographs of the NRHs. (c) Absorption (blue) and emission (red) spectra of NRHs. Inset shows a magnified view of the emission spectral region. (d) Direct intraband hole absorption mechanism of upconversion where an intraband absorption (1) allows the hole to transfer cross to the second dot (2). (e) Auger-mediated upconversion mechanism where an Auger recombination after a second interband absorption event (1) leads to the formation of a hot hole (2), which then gets transferred to the second dot (3).[65] Reproduced with permission from ref 65. Copyright 2013 Springer Nature.

NRH will bring its size, composition, and surface dependent properties that can be coupled together for synergistic effects.

For example, size and composition dependent optical properties can be exploited to tune the desired spectral range of absorption and emission while band alignment can be engineered to enable charge separation, recombination, and/or extraction. NRHs have been examined as absorbers and charge separation centers in photovoltaics.[23,58,59,142−144] Efficient luminescence upconversion has been demonstrated in dot-in-rods with an additional semiconductor grown at one tip.[65,66,141] Double heterojunctions achieved by selective ZnSe growth on CdSe/CdS/CdSe barbell structures have led to light-emitting diodes that can also function as photodetectors/photovoltaics, paving the path for new directions in multifunctional displays.[144] Near-infrared localized surface plasmon resonance can also be integrated with band structure engineering utilizing NRHs that include materials such as $Cu_{2-x}S$ as one of their components.[40,42,145,146] Especially with metal nanoparticles deposited on them, NRHs have been explored as potential photocatalysts for solar energy conversion as well.[147−149] Among these many potential directions, we highlight below two selected promising examples of applications of NRHs that have been explored.

4.1. Luminescence Upconversion

The ability to engineer band gaps and alignment in NRHs provides many opportunities in electronic, photonic, and optoelectronic applications. One such direction being explored is luminescence upconversion. Materials that can convert two low-energy photons into one high-energy photon can be highly beneficial in many applications. Upconverters can allow below-band gap photons that would otherwise have been lost to be absorbed by solar cells.[150,151] They can also find use in biomedical imaging and therapies using near-infrared radiation that can penetrate deeper into the skin.[152,153] NRHs provide the opportunities to develop color tunable upconverters using established concepts in band structure engineering in semiconductors.

The main NRH examined for luminescence upconversion has been the extension of dot-in-rod structures, in particular, CdSe grown on one tip of Te-doped CdSe dot in CdS rod.

Figure 25 shows such a NRH with the expected band diagram, TEM images, absorption and photoluminescence spectra, and possible mechanisms of photon upconversion. The smaller band gap Te-doped CdSe dot acts as the absorber and the larger band gap CdSe tip serves as the shorter wavelength emitter.[65] Possible mechanisms include intraband absorption (Figure 25d) to generate the hot hole, followed by transfer to the emitter where radiative recombination occurs in the larger band gap material with a higher energy photon. The other potential mechanism depicted is the Auger-mediated process where the hot hole is generated by Auger recombination and again transfers to the large gap emitter for radiative recombination. The former intraband absorption mechanism has been identified as the working mechanism based on pump−probe and single particle upconversion measurements. Luminescence upconversion efficiency comparable to rare earth doped systems has also been reported.[65]

This NRH system for luminescence upconversion has also been shown to be advantageous over its spherical core/shell counterpart. In particular, better spatial separation of electrons and holes in NRHs than in the core/shell structures, afforded

https://doi.org/10.1021/acs.chemrev.2c00410
Chem. Rev. XXXX, XXX, XXX−XXX

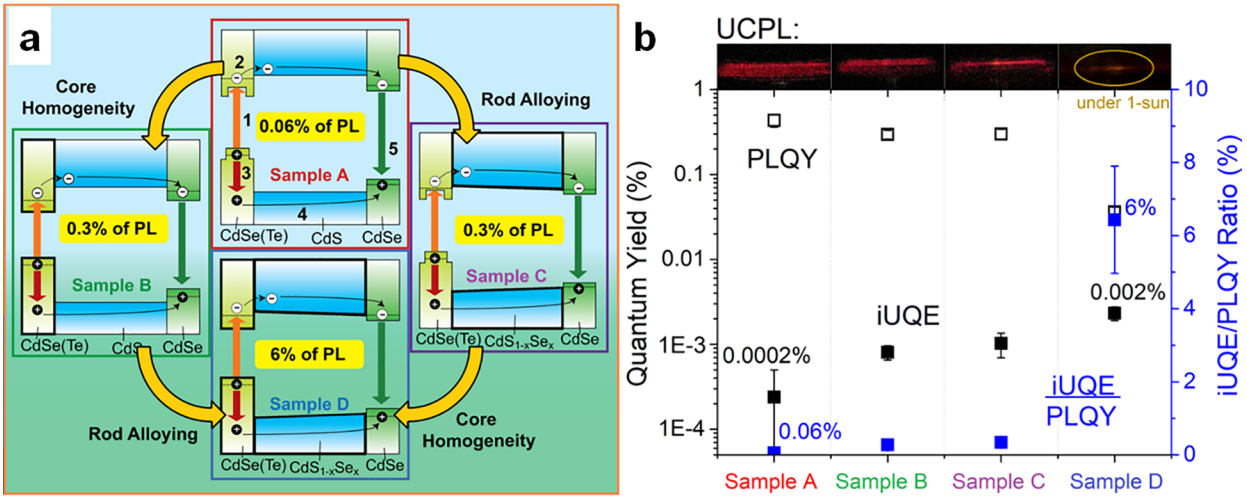

Figure 26. (a) Band diagrams representing four NRHs that illustrate the effects of core and rod alloying. The ratio of the internal upconversion quantum efficiency (iUQE) to the photoluminescence quantum yield (PLQY) are highlighted in yellow. (b) PLQY, iUQE, and corresponding iUQE/PLQY ratio for the four NRHs. Top inset: photographs of upconversion in NRH solutions (under 0.1 W cm^{-2} 750 nm CW excitation with a 650 and 700 nm short-pass).[141]

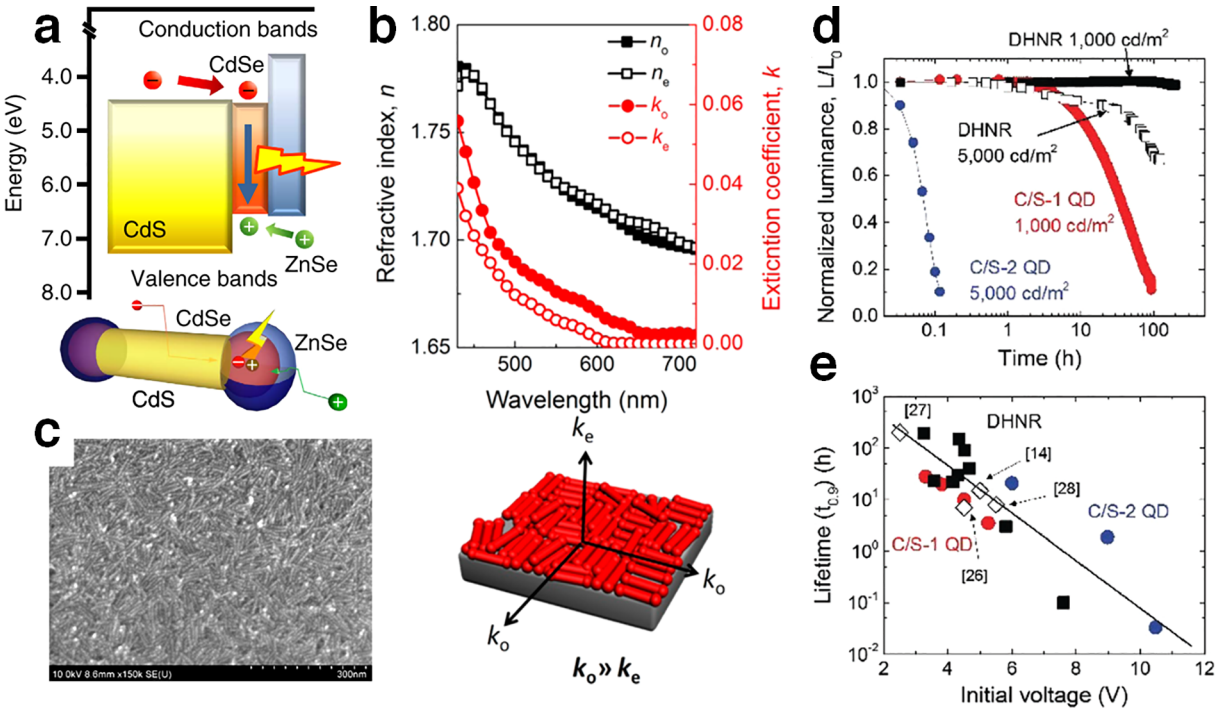

Figure 27. (a) Band diagram and schematic of double heterojunction nanorods (DHNRs).[60] (b) Ordinary (in-plane) and extraordinary (out-of-plane) components of real (n_o and n_e, respectively) and imaginary (k_o and k_e, respectively) parts of the refractive index and the corresponding schematic of a DHNR film.[139] (c) SEM image of a DHNR film.[60] (d) Luminance change over time of DHNR-LEDs (open and filled black squares) compared to that of core/shell QD-LEDs (red and blue circles) at constant current. The initial luminance of each device is indicated. (e) Initial driving voltage dependence of device lifetime to 90% of the initial luminance of DHNR-LEDs (filled squares) and core/shell QD-LEDs (red and blue circles). (d,e) Reproduced with permission from ref 158. Copyright 2017 Royal Society of Chemistry.

by the strategic placement of electron- and hole-preferred components near the opposite ends of the nanorods, has been suggested to be the key advantage.[66] By optimizing band gaps and alignment and through graded alloying (or possibly through diameter modulation) of the rod component of the NRH to enhance hot hole transfer to the larger band gap emitter, the possibility of improving luminescence upconversion by 2 orders of magnitude has been suggested.[141] Figure 26a illustrates the optimization of NRH's band gaps and alignment, while Figure 26b shows the corresponding improvement in luminescence upconversion. While these upconversion efficiencies appear relatively low, they should be considered within the context of the excitation condition, which is two-color continuous wave excitation at solar-relevant fluences. Note that the PLQY of the NRHs examined in this study is quite low. The upconversion efficiency normalized to PLQY is then supposed to factor out losses due to nonradiative recombination and therefore represents the potential improve-

https://doi.org/10.1021/acs.chemrev.2c00410
Chem. Rev. XXXX, XXX, XXX−XXX

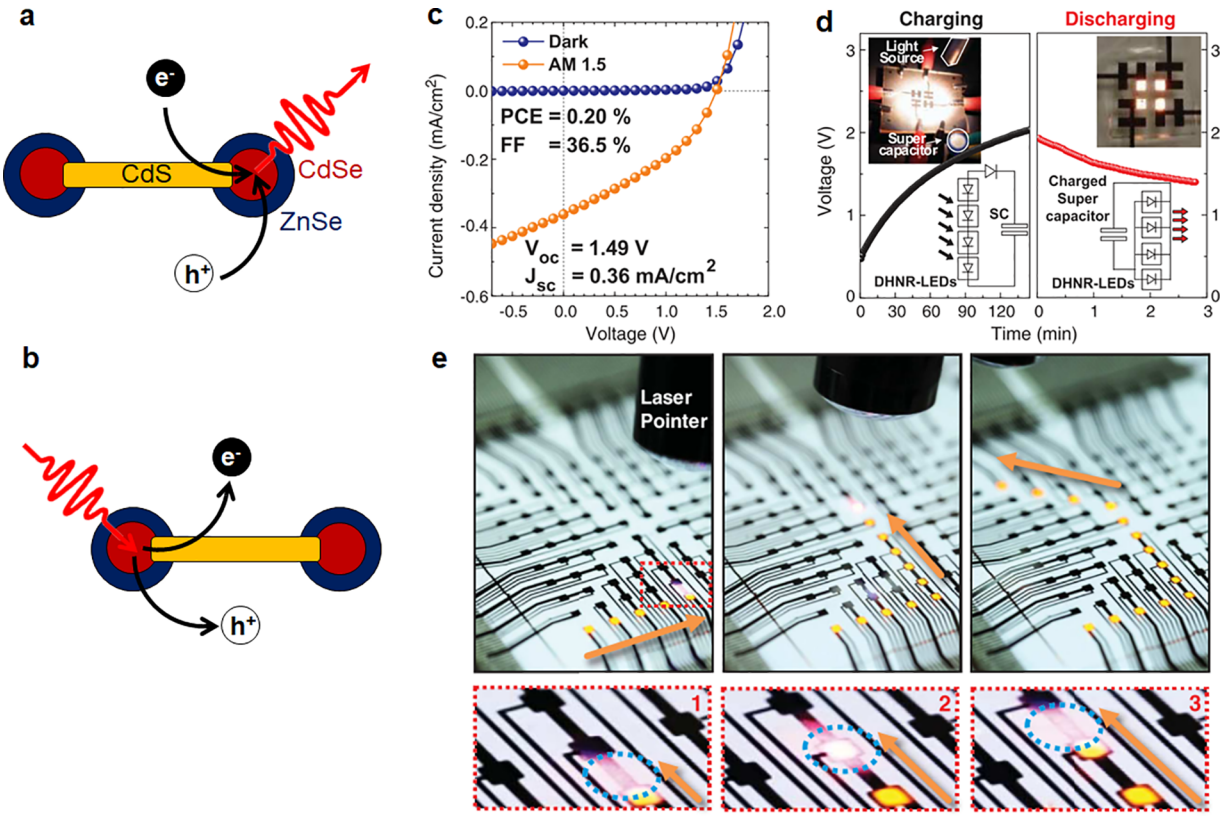

Figure 28. Schematics of CdS/CdSe/ZnSe DHNRs enabling efficient charge injection for electroluminescence (a) and efficient charge extraction for photocurrent generation (b) in the same device. (c) Dark- and photo- (under 100 mW cm^{-2} AM 1.5) current density *versus* voltage characteristics of a light-harvesting DHNR-LED. PCE, power conversion efficiency; FF, fill factor; V_{oc}, open-circuit voltage; J_{sc}, short-circuit current density.[144] (d) Time-dependent voltage curves of a supercapacitor (SC) being charged by and powering DHNR-LEDs. Corresponding circuit diagram and photograph of the LEDs are shown in the insets.[144] (e) Photographs of pixels in a light-responsive DHNR LED array turning on upon illumination with a laser pointer.[144]

ment in the actual upconversion process, leading to an expected upconversion efficiency of up to 6%. Furthermore, the use of semiconductor materials allows broad spectral absorption and quantum confinement effect facilitates tuning of both the absorption and emission energies. Hence, with further band structure design, optimization, and improved surface passivation, highly efficient luminescence upconversion materials can be envisioned from NRHs that allow precise engineering of both geometric and electronic structure.

4.2. Double Heterojunction Nanorods and Multifunctional Devices

Much of today's technology is enabled by devices that can carry out multiple tasks, including sensing and communicating. The pervasiveness of the smartphone exemplifies the advantages of and the demand for such multifunctional electronics. The smartphone can act as a video recorder, fingerprint scanner, high-definition display, *etc.*, with computing power that rivals larger computers of only a few years ago. All of these features must be implemented in a compact and lightweight platform. However, each added capability usually requires a new component or a whole new set of components that will increase weight, volume, complexity in manufacturing, and energy consumption both in production and in use. Developing materials that can impart multiple functionality within the same device component represents a potential solution to this challenge. NRHs can embody such an ability with advances in synthesis that allow precise engineering of band structure and directionality.

The barbell shaped NRHs with selective shell growth, also referred to as double heterojunction nanorods (DHNRs), represent the emergence of such tailored materials. DHNRs consist of a semiconductor quantum dot placed within a NRH with larger band gap materials, as illustrated in Figure 27a.[60] The larger band gap materials exhibit a staggered offset with respect to each other (type-II alignment) and straddling off set with the quantum dot (type-I). The two distinct outer materials (here CdS and ZnSe), both in contact with the emitting core (CdSe) within the rod geometry, allow directionality and tuning of barriers for electrons and holes independently. The presence of two quantum dots, rather than only one, is due to the ease of synthesis of the barbell structure.

When incorporated into a light-emitting diode (LED) structure, DHNRs can improve both the device efficiency and long-term stability. DHNRs can enhance external quantum efficiency by raising the ceiling on the light outcoupling limit due to the built-in anisotropy.[139] Because DHNRs lie flat when deposited into a film as verified by ellipsometry and SEM imaging (Figure 27b,c), DHNRs have a dipole orientation parallel to the substrate.[60,139] This orientation is then expected to lead to about a 2-fold increase in the light outcoupling limit,[154] which currently sets the ceiling on the maximum external quantum efficiencies of the core/shell quantum dot LEDs to ~20%.[7,155−157] At the same time, the double heterojunction band structure designed into DHNRs improves

https://doi.org/10.1021/acs.chemrev.2c00410
Chem. Rev. XXXX, XXX, XXX−XXX

device lifetime by allowing lower voltage operation for equivalent brightness (Figure 27d,e).[158]

In addition to the benefits in device efficiency and lifetime, the DHNR-LED can function both as a light source and as a photodetector/solar cell. The band alignment of the asymmetric shell surrounding the emitting core designed into DHNRs enables this capability. In DHNRs, two distinct materials that surround the quantum dot provide asymmetric barriers that facilitate injection and extraction of both types of charge carriers, allowing DHNR-LEDs to act as photodetector/photovoltaics without any modification to the device (Figure 28). Patterning an array of LED pixels that can simultaneously emit and detect/harvest light (*e.g.*, as in an emissive display, the feasibility of which is shown by a 10-by-10 pixel array in Figure 28e) can even allow additional capabilities such as bidirectional communication, touchless user interactivity, and ambient light harvesting, all without needing to introduce new components.

5. OUTLOOK

The development of colloidal NRHs is primed for rapid advancement. Serendipitous discoveries of unusual structures, often with disconnected understanding, are now being connected to establish a fuller, more unified picture of growth mechanisms. Along with this deeper understanding, developing approaches and tools to control factors that determine the underlying mechanisms as independently as possible will illuminate rational and precise synthetic routes to NRHs with properties that can be tailored in many ways.

The immediate challenge is to identify and quantify the roles of various thermodynamic and kinetic factors in nucleation and growth of complex heterogeneous systems. Building on this foundational knowledge will facilitate designing synthetic approaches to anisotropic nanocrystal heterostructures with tailored properties. Achieving tight control over size and size distribution has been a major enabling advance for single-composition and core/shell nanocrystals, especially given that one of their major appeals has been the size-dependent properties. An equivalent feat for NRHs will require overcoming a bigger hurdle of variations in shape/morphology and composition in addition to size. Multiple compositions and large surface-to-volume-ratio within each NRH also represent a considerable challenge in the optimization of their surface passivation to improve, for example, optical properties. Additionally, some phases which are useful for the production of NRHs can be "defective" or leave defects behind (*e.g.*, substoichiometric $Cu_{2-x}S$ or impurities left over after the cation exchange process) and can lead to less-than-ideal quality in structure and properties.[69] Beyond improving desired characteristics at the individual NRH level, alignment/ordered arrangement at large length scales may be desirable and can impose specific shape and ligand chemistry needs.

While these are significant and complex challenges, they also represent opportunities. Cu_2S is one of the earliest known semiconductors, but the highly mobile cations have limited its use in electronics. That exact disadvantage is now being exploited for efficient cation exchange in nanocrystals, opening up new avenues of research and generating a wealth of unprecedented combinations of composition, morphology, and properties. Even defective phases and impurity leftovers are helping to forge new directions (*e.g.*, localized surface plasmon resonance in $Cu_{2-x}S$ nanoparticles and doping effects of impurities leftover from cation exchange). Different surface compositions exhibited by anisotropic nanocrystal heterostructures may appear to complicate optimizing surface passivation (*e.g.*, for improving PL). However, they may also be exploited to impart regioselective ligand adsorption, providing variable surface chemistry that can potentially be used for programmable assembly of these complex nanocrystals.

Hence, the understanding of growth mechanisms and the improvement in synthetic capabilities that result from it will be the foundation for the predictable synthesis of not only individual but also hierarchical structures with increasing complexity. Efficient charge separation and luminescence upconversion are promising examples of benefits from one of the most rudimentary of anisotropic nanocrystal heterostructures. Devices with multiple functionality are also being enabled by anisotropic nanocrystal heterostructures. DHNR-LEDs have been shown to be capable of not only emitting but also detecting and harvesting light and may pave an energy-efficient path to meet the ever-increasing demand for high-performance smartphones, tablets, and other devices that have to function in multiple capacities in a compact, lightweight format.[144] These desirable characteristics demonstrated thus far are from only a single structure type (*i.e.*, QDs at the ends of a nanorod) and are just the tip of the iceberg of the capabilities that can be achieved in anisotropic nanocrysal heterostructures.

The focus of this review has been limited to solution heteroepitaxy and cation exchange starting from sphere or rod geometry. Other approaches such as oriented attachment[159] can open up new routes to essentially an unlimited number of configurations and morphologies with a wide variety of combinations of compositions. We finally note that continued advances in high-/atomic-resolution characterization with high throughput are necessary for the design and synthesis of complex-yet-well-defined anisotropic nanocrystal heterostructures before they can be integrated into the next generation of devices for optoelectronics, photonics, energy conversion, and beyond. As more calculated approaches to the synthesis of sophisticated and well-controlled NRHs become established, many application prospects that have not yet been considered will certainly emerge. We foresee a future where the design requirements of numerous specific applications will be met by anisotropic nanocrystal heterostructures synthesized with controlled number, size, shape, location, and orientation of constituent phases.

AUTHOR INFORMATION

Corresponding Author

Moonsub Shim − *Department of Materials Science and Engineering, University of Illinois at Urbana−Champaign, Urbana, Illinois 61801, United States;* orcid.org/0000-0001-7781-1029; Email: mshim@illinois.edu

Authors

Gryphon A. Drake − *Department of Materials Science and Engineering, University of Illinois at Urbana−Champaign, Urbana, Illinois 61801, United States;* orcid.org/0000-0002-4602-7562

Logan P. Keating − *Department of Materials Science and Engineering, University of Illinois at Urbana−Champaign, Urbana, Illinois 61801, United States;* orcid.org/0000-0002-1106-9658

https://doi.org/10.1021/acs.chemrev.2c00410
Chem. Rev. XXXX, XXX, XXX−XXX

Complete contact information is available at:
https://pubs.acs.org/10.1021/acs.chemrev.2c00410

Notes

The authors declare no competing financial interest.

Biographies

Gryphon A. Drake is a Ph.D. student working with Prof. Moonsub Shim at the University of Illinois Urbana−Champaign. He received dual B.S. degrees in Materials Science and Engineering and Biomedical Engineering from Carnegie Mellon University in 2014, where he studied nanoscale carbon−metal composites with Prof. Chris Pistorius. After graduation, he worked at the United States Naval Research Laboratory, developing infrared optical materials. He joined the Shim group in 2015 and received his M.S. degree in 2017, specializing in the intricate design of II−VI colloidal nanorod heterostructures.

Logan P. Keating is a Ph.D. student in the Shim group at the University of Illinois at Urbana−Champaign. He received his B.S. degree in Chemistry from Indiana University in 2016, where he did research in the Smith group on low-coordination iron complexes. His current research focuses on the growth of Cu-based nanorods and heterostructures, along with advanced electrical characterization of QD-LEDs.

Moonsub Shim is a professor of Materials Science and Engineering at the University of Illinois at Urbana−Champaign. He received his B.S. degree in Chemistry from the University of California at Berkeley in 1997 and his M.S. and Ph.D. degrees, both from the University of Chicago in 1998 and 2001. After working as a postdoctoral researcher at Stanford University, he joined the faculty of the Department of Materials Science and Engineering at Illinois in 2002. His research group's efforts revolve around nanoscale materials, especially heterostructures, spanning materials synthesis to charging and charge-separation processes to their applications in electronics, optoelectronics, and photovoltaics.

ACKNOWLEDGMENTS

Financial support from the U.S. National Science Foundation (grant nos. 1808163, 1825356, and 2132538) is gratefully acknowledged.

REFERENCES

(1) Hines, M. A.; Guyot-Sionnest, P. Synthesis and Characterization of Strongly Luminescing ZnS-Capped CdSe Nanocrystals. *J. Phys. Chem.* **1996**, *100*, 468−471.
(2) Dabbousi, B. O.; Rodriguez-Viejo, J.; Mikulec, F. V.; Heine, J. R.; Mattoussi, H.; Ober, R.; Jensen, K. F.; Bawendi, M. G. (CdSe)ZnS Core-Shell Quantum Dots: Synthesis and Characterization of a Size Series of Highly Luminescent Nanocrystallites. *J. Phys. Chem. B* **1997**, *101*, 9463−9475.
(3) Kim, S.; Fisher, B.; Eisler, H.-J.; Bawendi, M. Type-II Quantum Dots: CdTe/CdSe (Core/Shell) and CdSe/ZnTe (Core/Shell) Heterostructures. *J. Am. Chem. Soc.* **2003**, *125*, 11466−11467.
(4) Chen, O.; Zhao, J.; Chauhan, V. P.; Cui, J.; Wong, C.; Harris, D. K.; Wei, H.; Han, H. S.; Fukumura, D.; Jain, R. K.; Bawendi, M. G. Compact High-Quality CdSe-CdS Core-Shell Nanocrystals with Narrow Emission Linewidths and Suppressed Blinking. *Nat. Mater.* **2013**, *12*, 445−451.
(5) Zhou, J.; Zhu, M.; Meng, R.; Qin, H.; Peng, X. Ideal CdSe/CdS Core/Shell Nanocrystals Enabled by Entropic Ligands and Their Core Size-, Shell Thickness-, and Ligand-Dependent Photoluminescence Properties. *J. Am. Chem. Soc.* **2017**, *139*, 16556−16567.
(6) Park, Y. S.; Lim, J.; Klimov, V. I. Asymmetrically Strained Quantum Dots with Non-Fluctuating Single-Dot Emission Spectra and Subthermal Room-Temperature Linewidths. *Nat. Mater.* **2019**, *18*, 249−255.
(7) Won, Y. H.; Cho, O.; Kim, T.; Chung, D. Y.; Kim, T.; Chung, H.; Jang, H.; Lee, J.; Kim, D.; Jang, E. Highly Efficient and Stable InP/ZnSe/ZnS Quantum Dot Light-Emitting Diodes. *Nature* **2019**, *575*, 634−638.
(8) Chen, H.; He, J.; Wu, S. Recent Advances on Quantum-Dot-Enhanced Liquid-Crystal Displays. *IEEE J. Sel. Top. Quantum Electron.* **2017**, *23*, 1−11.
(9) Choi, M. K.; Yang, J.; Hyeon, T.; Kim, D. H. Flexible Quantum Dot Light-Emitting Diodes for Next-Generation Displays. *npj Flexible Electron* **2018**, *2*, 10.
(10) Martynenko, I. V.; Litvin, A. P.; Purcell-Milton, F.; Baranov, A. V.; Fedorov, A. V.; Gun'Ko, Y. K. Application of Semiconductor Quantum Dots in Bioimaging and Biosensing. *J. Mater. Chem. B* **2017**, *5*, 6701−6727.
(11) Kagan, C. R.; Lifshitz, E.; Sargent, E. H.; Talapin, D. V. Building Devices from Colloidal Quantum Dots. *Science* **2016**, *353*, aac5523.
(12) Hu, L.; Zhao, Q.; Huang, S.; Zheng, J.; Guan, X.; Patterson, R.; Kim, J.; Shi, L.; Lin, C.-H.; Lei, Q.; et al. Flexible and Efficient Perovskite Quantum Dot Solar Cells via Hybrid Interfacial Architecture. *Nat. Commun.* **2021**, *12*, 466.
(13) Kirmani, A. R.; Luther, J. M.; Abolhasani, M.; Amassian, A. Colloidal Quantum Dot Photovoltaics: Current Progress and Path to Gigawatt Scale Enabled by Smart Manufacturing. *ACS Energy Lett.* **2020**, *5*, 3069−3100.
(14) Park, Y. S.; Roh, J.; Diroll, B. T.; Schaller, R. D.; Klimov, V. I. Colloidal Quantum Dot Lasers. *Nat. Rev. Mater.* **2021**, *6*, 382−401.
(15) Kim, J.; Song, S.; Kim, Y.-H.; Park, S. K. Recent Progress of Quantum Dot-Based Photonic Devices and Systems: A Comprehensive Review of Materials, Devices, and Applications. *Small Struct* **2021**, *2*, 2000024.
(16) Bang, S. Y.; Suh, Y. H.; Fan, X. B.; Shin, D. W.; Lee, S.; Choi, H. W.; Lee, T. H.; Yang, J.; Zhan, S.; Harden-Chaters, W.; Samarakoon, C.; Occhipinti, L. G.; Han, S. D.; Jung, S. M.; Kim, J. M. Technology Progress on Quantum Dot Light-Emitting Diodes for Next-Generation Displays. *Nanoscale Horiz* **2021**, *6*, 68−77.
(17) Enright, M. J.; Cossairt, B. M. Synthesis of Tailor-Made Colloidal Semiconductor Heterostructures. *Chem. Commun.* **2018**, *54*, 7109−7122.
(18) Jiang, Y.; Cho, S. Y.; Shim, M. Light-Emitting Diodes of Colloidal Quantum Dots and Nanorod Heterostructures for Future Emissive Displays. *J. Mater. Chem. C* **2018**, *6*, 2618−2634.
(19) Kim, W. D.; Kim, D.; Yoon, D. E.; Lee, H.; Lim, J.; Bae, W. K.; Lee, D. C. Pushing the Efficiency Envelope for Semiconductor Nanocrystal-Based Electroluminescence Devices Using Anisotropic Nanocrystals. *Chem. Mater.* **2019**, *31*, 3066−3082.
(20) Xu, L.; Liang, H. W.; Yang, Y.; Yu, S. H. Stability and Reactivity: Positive and Negative Aspects for Nanoparticle Processing. *Chem. Rev.* **2018**, *118*, 3209−3250.
(21) Beberwyck, B. J.; Surendranath, Y.; Alivisatos, A. P. Cation Exchange: A Versatile Tool for Nanomaterials Synthesis. *J. Phys. Chem. C* **2013**, *117*, 19759−19770.
(22) Steimle, B. C.; Fenton, J. L.; Schaak, R. E. Rational Construction of a Scalable Heterostructured Nanorod Megalibrary. *Science* **2020**, *367*, 418−424.
(23) Flanagan, J. C.; Keating, L. P.; Kalasad, M. N.; Shim, M. Extending the Spectral Range of Double-Heterojunction Nanorods by Cation Exchange-Induced Alloying. *Chem. Mater.* **2019**, *31*, 9307−9316.
(24) Bauer, E. Phänomenologische Theorie der Kristallabscheidung an Oberflächen. I. *Zeitschrift Kristallogr.*. **1958**, *110*, 372−394.
(25) Abe, S.; Capek, R. K.; De Geyter, B.; Hens, Z. Reaction Chemistry/Nanocrystal Property Relations in the Hot Injection Synthesis, the Role of the Solute Solubility. *ACS Nano* **2013**, *7*, 943−949.

(26) Oh, N.; Shim, M. Metal Oleate Induced Etching and Growth of Semiconductor Nanocrystals, Nanorods, and Their Heterostructures. *J. Am. Chem. Soc.* **2016**, *138*, 10444−10451.
(27) Ji, B.; Panfil, Y. E.; Waiskopf, N.; Remennik, S.; Popov, I.; Banin, U. Strain-Controlled Shell Morphology on Quantum Rods. *Nat. Commun.* **2019**, *10*, 2.
(28) Shim, M.; McDaniel, H.; Oh, N. Prospects for Strained Type-II Nanorod Heterostructures. *J. Phys. Chem. Lett.* **2011**, *2*, 2722−2727.
(29) Demortière, A.; Leonard, D. N.; Petkov, V.; Chapman, K.; Chattopadhyay, S.; She, C.; Cullen, D. A.; Shibata, T.; Pelton, M.; Shevchenko, E. V. Strain-Driven Stacking Faults in CdSe/CdS Core/Shell Nanorods. *J. Phys. Chem. Lett.* **2018**, *9*, 1900−1906.
(30) Enders, F.; Budweg, A.; Zeng, P.; Lauth, J.; Smith, T. A.; Brida, D.; Boldt, K. Switchable Dissociation of Excitons Bound at Strained CdTe/CdS Interfaces. *Nanoscale* **2018**, *10*, 22362−22373.
(31) Kim, D.; Shcherbakov-Wu, W.; Ha, S. K.; Lee, W. S.; Tisdale, W. A. Uniaxial Strain Engineering Via Core Position Control in CdSe/CdS Core/Shell Nanorods and Their Optical Response. *ACS Nano* **2022**, *16*, 14713−14722.
(32) Kim, D.; Lee, Y. K.; Lee, D.; Kim, W. D.; Bae, W. K.; Lee, D. C. Colloidal Dual-Diameter and Core-Position-Controlled Core/Shell Cadmium Chalcogenide Nanorods. *ACS Nano* **2017**, *11*, 12461−12472.
(33) Ruberu, T. P. A.; Albright, H. R.; Callis, B.; Ward, B.; Cisneros, J.; Fan, H.-j.; Vela, J. Molecular Control of the Nanoscale: Effect of Phosphine-Chalcogenide Reactivity on CdS-CdSe Nanocrystal Composition and Morphology. *ACS Nano* **2012**, *6*, 5348−5359.
(34) Frenette, L. C.; Krauss, T. D. Uncovering Active Precursors in Colloidal Quantum Dot Synthesis. *Nat. Commun.* **2017**, *8*, 2082.
(35) Hoshino, S. Structure and Dynamics of Solid State Ionics. *Solid State Ionics* **1991**, *48*, 179−201.
(36) Tubandt, C.; Lorenz, E. Molekularzustand und Elektrisches Leitvermögen Kristallisierter Salze. *Zeitschrift für Phys. Chemie* **1914**, *87U*, 513−542.
(37) Wang, L.-W. High Chalcocite Cu_2S: A Solid-Liquid Hybrid Phase. *Phys. Rev. Lett.* **2012**, *108*, 085703.
(38) Wakamura, K. Small Band Gap and High Ionic Conduction in Cu_2S. *Solid State Ionics* **2000**, *130*, 305−312.
(39) Danilkin, S. A.; Skomorokhov, A. N.; Hoser, A.; Fuess, H.; Rajevac, V.; Bickulova, N. N. Crystal Structure and Lattice Dynamics of Superionic Copper Selenide $Cu_{2-\delta}Se$. *J. Alloys Compd.* **2003**, *361*, 57−61.
(40) Zhai, Y.; Shim, M. Cu_2S/ZnS Heterostructured Nanorods: Cation Exchange vs. Solution−Liquid−Solid-Like Growth. *ChemPhysChem* **2016**, *17*, 741−751.
(41) Mu, L.; Wang, F.; Sadtler, B.; Loomis, R. A.; Buhro, W. E. Influence of the Nanoscale Kirkendall Effect on the Morphology of Copper Indium Disulfide Nanoplatelets Synthesized by Ion Exchange. *ACS Nano* **2015**, *9*, 7419−7428.
(42) Zhai, Y.; Flanagan, J. C.; Shim, M. Lattice Strain and Ligand Effects on the Formation of $Cu_{2-x}S$/I-III-VI_2 Nanorod Heterostructures Through Partial Cation Exchange. *Chem. Mater.* **2017**, *29*, 6161−6167.
(43) De Trizio, L.; Gaspari, R.; Bertoni, G.; Kriegel, I.; Moretti, L.; Scotognella, F.; Maserati, L.; Zhang, Y.; Messina, G. C.; Prato, M.; Marras, S.; Cavalli, A.; Manna, L. $Cu_{3-X}P$ Nanocrystals as a Material Platform for Near-Infrared Plasmonics and Cation Exchange Reactions. *Chem. Mater.* **2015**, *27*, 1120−1128.
(44) Manna, L.; Scher, E. C.; Alivisatos, A. P. Synthesis of Soluble and Processable Rod-, Arrow-, Teardrop-, and Tetrapod-Shaped CdSe Nanocrystals. *J. Am. Chem. Soc.* **2000**, *122*, 12700−12706.
(45) Peng, X.; Manna, L.; Yang, W.; Wickham, J.; Scher, E.; Kadavanich, A.; Alivisatos, A. P. Shape Control of CdSe Nanocrystals. *Nature* **2000**, *404*, 59−61.
(46) Peng, Z. A.; Peng, X. Mechanisms of the Shape Evolution of CdSe Nanocrystals. *J. Am. Chem. Soc.* **2001**, *123*, 1389−1395.
(47) Manna, L.; Milliron, D. J.; Meisel, A.; Scher, E. C.; Alivisatos, A. P. Controlled Growth of Tetrapod-Branched Inorganic Nanocrystals. *Nat. Mater.* **2003**, *2*, 382−385.
(48) Talapin, D. V.; Koeppe, R.; Götzinger, S.; Kornowski, A.; Lupton, J. M.; Rogach, A. L.; Benson, O.; Feldmann, J.; Weller, H. Highly Emissive Colloidal CdSe/CdS Heterostructures of Mixed Dimensionality. *Nano Lett.* **2003**, *3*, 1677−1681.
(49) Talapin, D. V.; Nelson, J. H.; Shevchenko, E. V.; Aloni, S.; Sadtler, B.; Alivisatos, A. P. Seeded Growth of Highly Luminescent CdSe/CdS Nanoheterostructures with Rod and Tetrapod Morphologies. *Nano Lett.* **2007**, *7*, 2951−2959.
(50) Carbone, L.; et al. Synthesis and Micrometer-Scale Assembly of Colloidal CdSe/CdS Nanorods Prepared by a Seeded Growth Approach. *Nano Lett.* **2007**, *7*, 2942−2950.
(51) Wu, K.; Hill, L. J.; Chen, J.; McBride, J. R.; Pavlopolous, N. G.; Richey, N. E.; Pyun, J.; Lian, T. Universal Length Dependence of Rod-to-Seed Exciton Localization Efficiency in Type I and Quasi-Type II CdSe@CdS Nanorods. *ACS Nano* **2015**, *9*, 4591−4599.
(52) Halpert, J. E.; Porter, V. J.; Zimmer, J. P.; Bawendi, M. G. Synthesis of CdSe/CdTe Nanobarbells. *J. Am. Chem. Soc.* **2006**, *128*, 12590−12591.
(53) Kumar, S.; Jones, M.; Lo, S. S.; Scholes, G. D. Nanorod Heterostructures Showing Photoinduced Charge Separation. *Small* **2007**, *3*, 1633−1639.
(54) Saunders, A. E.; Koo, B.; Wang, X.; Shih, C. K.; Korgel, B. A. Structural Characterization and Temperature-Dependent Photoluminescence of Linear CdTe/CdSe/CdTe Heterostructure Nanorods. *ChemPhysChem* **2008**, *9*, 1158−1163.
(55) Mcdaniel, H.; Zuo, J.-m.; Shim, M. Anisotropic Strain-Induced Curvature in Type-II CdSe/CdTe. *J. Am. Chem. Soc.* **2010**, *132*, 3286−3288.
(56) McDaniel, H.; Oh, N.; Shim, M. CdSe-$CdSe_xTe_{1-x}$ Nanorod Heterostructures: Tuning Alloy Composition and Spatially Indirect Recombination Energies. *J. Mater. Chem.* **2012**, *22*, 11621−11628.
(57) McDaniel, H.; Pelton, M.; Oh, N.; Shim, M. Effects of Lattice Strain and Band Offset on Electron Transfer Rates in Type-II Nanorod Heterostructures. *J. Phys. Chem. Lett.* **2012**, *3*, 1094−1098.
(58) Flanagan, J. C.; Shim, M. Enhanced Air Stability, Charge Separation, and Photocurrent in CdSe/CdTe Heterojunction Nanorods by Thiols. *J. Phys. Chem. C* **2015**, *119*, 20162−20168.
(59) Lee, S.; Flanagan, J. C.; Kim, J.; Yun, A. J.; Lee, B.; Shim, M.; Park, B. Efficient Type-II Heterojunction Nanorod Sensitized Solar Cells Realized by Controlled Synthesis of Core/Patchy-Shell Structure and CdS Cosensitization. *ACS Appl. Mater. Interfaces* **2019**, *11*, 19104−19114.
(60) Oh, N.; Nam, S.; Zhai, Y.; Deshpande, K.; Trefonas, P.; Shim, M. Double-Heterojunction Nanorods. *Nat. Commun.* **2014**, *5*, 3642.
(61) Drake, G. A.; Flanagan, J. C.; Shim, M. Highly Luminescent Double-Heterojunction Nanorods. *J. Chem. Phys.* **2019**, *151*, 134706.
(62) Ji, B.; Panfil, Y. E.; Banin, U. Heavy-Metal-Free Fluorescent ZnTe/ZnSe Nanodumbbells. *ACS Nano* **2017**, *11*, 7312−7320.
(63) Kirsanova, M.; Nemchinov, A.; Hewa-Kasakarage, N. N.; Schmall, N.; Zamkov, M. Synthesis of ZnSe/CdS/ZnSe Nanobarbells Showing Photoinduced Charge Separation. *Chem. Mater.* **2009**, *21*, 4305−4309.
(64) Enders, F.; Sutter, S.; Fischli, D.; Köser, R.; Monter, S.; Cardinal, S.; Boldt, K. Regioselective Growth Mechanism of Single Semiconductor Tips on CdS Nanorods. *Chem. Mater.* **2020**, *32*, 10566−10574.
(65) Deutsch, Z.; Neeman, L.; Oron, D. Luminescence Upconversion in Colloidal Double Quantum Dots. *Nat. Nanotechnol.* **2013**, *8*, 649−653.
(66) Chen, E. Y.; Li, Z.; Milleville, C. C.; Lennon, K. R.; Zide, J. M.; Doty, M. F. CdSe(Te)/CdS/CdSe Rods Versus CdTe/CdS/CdSe Spheres: Morphology-Dependent Carrier Dynamics for Photon Upconversion. *IEEE J. of Photovoltaics* **2018**, *8*, 746−751.
(67) Li, H.; Brescia, R.; Krahne, R.; Bertoni, G.; Alcocer, M. J.; D'Andrea, C.; Scotognella, F.; Tassone, F.; Zanella, M.; De Giorgi, M.; Manna, L. Blue-UV-Emitting ZnSe(Dot)/ZnS(Rod) Core/Shell Nanocrystals Prepared from CdSe/CdS Nanocrystals by Sequential Cation Exchange. *ACS Nano* **2012**, *6*, 1637−1647.

https://doi.org/10.1021/acs.chemrev.2c00410
Chem. Rev. XXXX, XXX, XXX−XXX

(68) Van Der Stam, W.; Bladt, E.; Rabouw, F. T.; Bals, S.; De Mello Donega, C. Near-Infrared Emitting $CuInSe_2/CuInS_2$ Dot Core/Rod Shell Heteronanorods by Sequential Cation Exchange. *ACS Nano* **2015**, *9*, 11430−11438.
(69) Coughlan, C.; Ibáñez, M.; Dobrozhan, O.; Singh, A.; Cabot, A.; Ryan, K. M. Compound Copper Chalcogenide Nanocrystals. *Chem. Rev.* **2017**, *117*, 5865−6109.
(70) Kapuria, N.; Ghorpade, U. V.; Zubair, M.; Mishra, M.; Singh, S.; Ryan, K. M. Metal Chalcogenide Semiconductor Nanocrystals Synthesized from Ion-Conducting Seeds and their Applications. *J. Mater. Chem. C* **2020**, *8*, 13868−13895.
(71) Keating, L. P.; Shim, M. Mechanism of Morphology Variations in Colloidal $CuGaS_2$ Nanorods. *Nanoscale Adv.* **2021**, *3*, 5322−5331.
(72) Oh, N.; Keating, L. P.; Drake, G. A.; Shim, M. $CuGaS_2$-$CuInE_2$ (E = S, Se) Colloidal Nanorod Heterostructures. *Chem. Mater.* **2019**, *31*, 1973−1980.
(73) Fiore, A.; Mastria, R.; Lupo, M. G.; Lanzani, G.; Giannini, C.; Carlino, E.; Morello, G.; De Giorgi, M.; Li, Y.; Cingolani, R.; Manna, L. Tetrapod-Shaped Colloidal Nanocrystals of II-VI Semiconductors Prepared by Seeded Growth. *J. Am. Chem. Soc.* **2009**, *131*, 2274−2282.
(74) Enright, M. J.; Dou, F. Y.; Wu, S.; Rabe, E. J.; Monahan, M.; Friedfeld, M. R.; Schlenker, C. W.; Cossairt, B. M. Seeded Growth of Nanoscale Semiconductor Tetrapods: Generality and the Role of Cation Exchange. *Chem. Mater.* **2020**, *32*, 4774−4784.
(75) Coropceanu, I.; Rossinelli, A.; Caram, J. R.; Freyria, F. S.; Bawendi, M. G. Slow-Injection Growth of Seeded CdSe/CdS Nanorods with Unity Fluorescence Quantum Yield and Complete Shell to Core Energy Transfer. *ACS Nano* **2016**, *10*, 3295−3301.
(76) Grennell, A. N.; Utterback, J. K.; Pearce, O. M.; Wilker, M. B.; Dukovic, G. Relationships Between Exciton Dissociation and Slow Recombination Within ZnSe/CdS and CdSe/CdS Dot-In-Rod Heterostructures. *Nano Lett.* **2017**, *17*, 3764−3774.
(77) She, C.; Demortière, A.; Shevchenko, E. V.; Pelton, M. Using Shape to Control Photoluminescence from CdSe/CdS Core/Shell Nanorods. *J. Phys. Chem. Lett.* **2011**, *2*, 1469−1475.
(78) Carbone, L.; Kudera, S.; Carlino, E.; Parak, W. J.; Giannini, C.; Cingolani, R.; Manna, L. Multiple Wurtzite Twinning in CdTe Nanocrystals Induced by Methylphosphonic Acid. *J. Am. Chem. Soc.* **2006**, *128*, 748−755.
(79) Bladt, E.; Van Dijk-Moes, R. J.; Peters, J.; Montanarella, F.; De Mello Donega, C.; Vanmaekelbergh, D.; Bals, S. Atomic Structure of Wurtzite CdSe (Core)/CdS (Giant Shell) Nanobullets Related to Epitaxy and Growth. *J. Am. Chem. Soc.* **2016**, *138*, 14288−14293.
(80) Puzder, A.; Williamson, A. J.; Zaitseva, N.; Galli, G.; Manna, L.; Alivisatos, A. P. The Effect of Organic Ligand Binding on the Growth of CdSe Nanoparticles Probed by Ab Initio Calculations. *Nano Lett.* **2004**, *4*, 2361−2365.
(81) Gomes, R.; Hassinen, A.; Szczygiel, A.; Zhao, Q.; Vantomme, A.; Martins, J. C.; Hens, Z. Binding of Phosphonic Acids to CdSe Quantum Dots: A Solution NMR Study. *J. Phys. Chem. Lett.* **2011**, *2*, 145−152.
(82) Tamukong, P. K.; Peiris, W. D.; Kilina, S. Computational Insights into CdSe Quantum Dots' Interactions with Acetate Ligands. *Phys. Chem. Chem. Phys.* **2016**, *18*, 20499−20510.
(83) Calvin, J. J.; Brewer, A. S.; Alivisatos, A. P. The Role of Organic Ligand Shell Structures in Colloidal Nanocrystal Synthesis. *Nat. Synth.* **2022**, *1*, 127−137.
(84) Shieh, F.; Saunders, A. E.; Korgel, B. A. General Shape Control of Colloidal CdS, CdSe, CdTe Quantum Rods and Quantum Rod Heterostructures. *J. Phys. Chem. B* **2005**, *109*, 8538−8542.
(85) Carbone, L.; Kudera, S.; Giannini, C.; Ciccarella, G.; Cingolani, R.; Cozzoli, P. D.; Manna, L. Selective Reactions on the Tips of Colloidal Semiconductor Nanorods. *J. Mater. Chem.* **2006**, *16*, 3952−3956.
(86) Milliron, D.; Hughes, S. M.; Cui, Y.; Manna, L.; Li, J.; Wang, L. W.; Alivisatos, A. P. Colloidal Nanocrystal Heterostructures with Linear and Branched Topology. *Nature* **2004**, *430*, 190−195.
(87) Kudera, S.; Carbone, L.; Casula, M. F.; Cingolani, R.; Falqui, A.; Snoeck, E.; Parak, W. J.; Manna, L. Selective Growth of PbSe on One or Both Tips of Colloidal Semiconductor Nanorods. *Nano Lett.* **2005**, *5*, 445−449.
(88) Mokari, T.; Banin, U. Synthesis and Properties of CdSe/ZnS Core/Shell Nanorods. *Chem. Mater.* **2003**, *15*, 3955−3960.
(89) Ning, J.; Xiong, Y.; Kershaw, S. V.; Rogach, A. L. Phase-Dependent Shell Growth and Optical Properties of ZnSe/ZnS Core/Shell Nanorods. *Chem. Mater.* **2021**, *33*, 3413−3427.
(90) Wang, W.; Banerjee, S.; Jia, S.; Steigerwald, M. L.; Herman, I. P. Ligand Control of Growth, Morphology, and Capping Structure of Colloidal CdSe Nanorods. *Chem. Mater.* **2007**, *19*, 2573−2580.
(91) Enright, M. J.; Sarsito, H.; Cossairt, B. M. Kinetically Controlled Assembly of Cadmium Chalcogenide Nanorods and Nanorod Heterostructures. *Mater. Chem. Front.* **2018**, *2*, 1296−1305.
(92) Drake, G. A. Controlling Structure and Composition in Double-Heterojunction Nanorods for High Quantum Yield and Tunable Color. Thesis. University of Illinois at Urbana−Champaign, 2017; http://hdl.handle.net/2142/98310 (accessed 2022-09).
(93) Voznyy, O.; Levina, L.; Fan, J. Z.; Askerka, M.; Jain, A.; Choi, M. J.; Ouellette, O.; Todorović, P.; Sagar, L. K.; Sargent, E. H. Machine Learning Accelerates Discovery of Optimal Colloidal Quantum Dot Synthesis. *ACS Nano* **2019**, *13*, 11122−11128.
(94) Baum, F.; Pretto, T.; Köche, A.; Santos, M. J. L. Machine Learning Tools to Predict Hot Injection Syntheses Outcomes for II-VI and IV-VI Quantum Dots. *J. Phys. Chem. C* **2020**, *124*, 24298−24305.
(95) Vikram, A.; Brudnak, K.; Zahid, A.; Shim, M.; Kenis, P. J. Accelerated Screening of Colloidal Nanocrystals Using Artificial Neural Network-Assisted Autonomous Flow Reactor Technology. *Nanoscale* **2021**, *13*, 17028−17039.
(96) De Trizio, L.; Manna, L. Forging Colloidal Nanostructures Via Cation Exchange Reactions. *Chem. Rev.* **2016**, *116*, 10852−10887.
(97) Brovelli, S.; Galland, C.; Viswanatha, R.; Klimov, V. I. Tuning Radiative Recombination in Cu-Doped Nanocrystals Via Electrochemical Control of Surface Trapping. *Nano Lett.* **2012**, *12*, 4372−4379.
(98) Yang, L.; Knowles, K. E.; Gopalan, A.; Hughes, K. E.; James, M. C.; Gamelin, D. R. One-Pot Synthesis of Monodisperse Colloidal Copper-Doped CdSe Nanocrystals Mediated by Ligand-Copper Interactions. *Chem. Mater.* **2016**, *28*, 7375−7384.
(99) Pearson, R. G. Hard and Soft Acids and Bases. *J. Am. Chem. Soc.* **1963**, *85*, 3533−3539.
(100) Li, H.; Zanella, M.; Genovese, A.; Povia, M.; Falqui, A.; Giannini, C.; Manna, L. Sequential Cation Exchange in Nanocrystals: Preservation of Crystal Phase and Formation of Metastable Phases. *Nano Lett.* **2011**, *11*, 4964−4970.
(101) Gan, X. Y.; Sen, R.; Millstone, J. E. Connecting Cation Exchange and Metal Deposition Outcomes Via Hume-Rothery-like Design Rules Using Copper Selenide Nanoparticles. *J. Am. Chem. Soc.* **2021**, *143*, 8137−8144.
(102) Dong, K.; Chen, Q. C.; Xing, Z.; Chen, Y.; Qi, Y.; Pavlpoulos, N. G.; Amirav, L. Silver Tipping of CdSe@CdS Nanorods: How to Avoid Cation Exchange. *Chem. Mater.* **2021**, *33*, 6394−6402.
(103) Oh, N.; Keating, L. P.; Drake, G. A.; Shim, M. $CuGaS_2$-$CuInE_2$ (E = S, Se) Colloidal Nanorod Heterostructures. *Chem. Mater.* **2019**, *31*, 1973−1980.
(104) Zhao, M.; Huang, F.; Lin, H.; Zhou, J.; Xu, J.; Wu, Q.; Wang, Y. $CuGaS_2$−ZnS p−n Nanoheterostructures: a Promising Visible Light Photo-Catalyst for Water-Splitting Hydrogen Production. *Nanoscale* **2016**, *8*, 16670−16676.
(105) Omata, T.; Nose, K.; Otsuka-Yao-Matsuo, S. Size Dependent Optical Band Gap of Ternary I-III-VI_2 Semiconductor Nanocrystals. *J. Appl. Phys.* **2009**, *105*, 073106.
(106) Wang, J.; Chen, K.; Gong, M.; Xu, B.; Yang, Q. Solution−Solid−Solid Mechanism: Superionic Conductors Catalyze Nanowire Growth. *Nano Lett.* **2013**, *13*, 3996−4000.

https://doi.org/10.1021/acs.chemrev.2c00410
Chem. Rev. XXXX, XXX, XXX−XXX

(107) Prusty, G.; Guria, A. K.; Patra, B. K.; Pradhan, N. Diffusion-Induced Shape Evolution in Multinary Semiconductor Nanostructures. *J. Phys. Chem. Lett.* **2015**, *6*, 2421−2426.
(108) Adhikari, S. D.; Dutta, A.; Prusty, G.; Sahu, P.; Pradhan, N. Symmetry Break and Seeded 2D Anisotropic Growth in Ternary $CuGaS_2$ Nanocrystals. *Chem. Mater.* **2017**, *29*, 5384−5393.
(109) Han, W.; Yi, L.; Zhao, N.; Tang, A.; Gao, M.; Tang, Z. Synthesis and Shape-Tailoring of Copper Sulfide/Indium Sulfide-Based Nanocrystals. *J. Am. Chem. Soc.* **2008**, *130*, 13152−13161.
(110) Xiao, N.; Zhu, L.; Wang, K.; Dai, Q.; Wang, Y.; Li, S.; Sui, Y.; Ma, Y.; Liu, J.; Liu, B.; Zou, G.; Zou, B. Synthesis and High-Pressure Transformation of Metastable Wurtzite-Structured $CuGaS_2$ Nanocrystals. *Nanoscale* **2012**, *4*, 7443.
(111) Yi, L.; Tang, A.; Niu, M.; Han, W.; Hou, Y.; Gao, M. Synthesis and Self-Assembly of $Cu_{1.94}S$−ZnS Heterostructured Nanorods. *CrystEngComm* **2010**, *12*, 4124−4130.
(112) Chang, J.-Y.; Cheng, C.-Y. Facile One-Pot Synthesis of Copper Sulfide−Metal Chalcogenide Anisotropic Heteronanostructures in a Noncoordinating Solvent. *Chem. Commun.* **2011**, *47*, 9089−9091.
(113) Choi, S.-H.; Kim, E.-G.; Hyeon, T. One-Pot Synthesis of Copper-Indium Sulfide Nanocrystal Heterostructures with Acorn, Bottle, and Larva Shapes. *J. Am. Chem. Soc.* **2006**, *128*, 2520−2521.
(114) Connor, S. T.; Hsu, C.-M.; Weil, B. D.; Aloni, S.; Cui, Y. Phase Transformation of Biphasic Cu_2S-$CuInS_2$ to Monophasic $CuInS_2$ Nanorods. *J. Am. Chem. Soc.* **2009**, *131*, 4962−4966.
(115) Kruszynska, M.; Borchert, H.; Parisi, J.; Kolny-Olesiak, J. Synthesis and Shape Control of $CuInS_2$ Nanoparticles. *J. Am. Chem. Soc.* **2010**, *132*, 15976−15986.
(116) Xia, C.; van Oversteeg, C. H. M.; Bogaards, V. C. L.; Spanjersberg, T. H. M.; Visser, N. L.; Berends, A. C.; Meeldijk, J. D.; de Jongh, P. E.; de Mello Donega, C. Synthesis and Formation Mechanism of Colloidal Janus-Type $Cu_{2-x}S$/$CuInS_2$ Heteronanorods via Seeded Injection. *ACS Nano* **2021**, *15*, 9987−9999.
(117) Li, J.; Bloemen, M.; Parisi, J.; Kolny-Olesiak, J. Role of Copper Sulfide Seeds in the Growth Process of $CuInS_2$ Nanorods and Networks. *ACS Appl. Mater. Interfaces* **2014**, *6*, 20535−20543.
(118) Li, Q.; Zhai, L.; Zou, C.; Huang, X.; Zhang, L.; Yang, Y.; Chen, X.; Huang, S. Wurtzite $CuInS_2$ and $CuIn_xGa_{1-x}S_2$ Nanoribbons: Synthesis, Optical and Photoelectrical Properties. *Nanoscale* **2013**, *5*, 1638.
(119) Geng, X.; Liu, H.; Zhai, L.; Xiong, Z.; Hu, J.; Zou, C.; Dong, Y.; Yang, Y.; Huang, S. Colloidal Synthesis of $CuGaS_xSe_{2-x}$ Nanoribbons Mediated by $Cu_{1.75}$(SSe) Nanocrystals as Catalysts. *J. Alloys Compd.* **2014**, *617*, 961−967.
(120) Zhou, J.; Huang, F.; Xu, J.; Wang, Y. $Cu_{1.94}S$−MnS Dimeric Nanoheterostructures with Bifunctions: Localized Surface Plasmon Resonance and Magnetism. *CrystEngComm* **2013**, *15*, 4217−4220.
(121) Zhang, W.; Zhai, L.; He, N.; Zou, C.; Geng, X.; Cheng, L.; Dong, Y.; Huang, S. Solution-Based Synthesis of Wurtzite Cu_2ZnSnS_4 Nanoleaves Introduced by α-Cu_2S Nanocrystals as a Catalyst. *Nanoscale* **2013**, *5*, 8114−8121.
(122) Chen, Y.; Zhao, S.; Wang, X.; Peng, Q.; Lin, R.; Wang, Y.; Shen, R.; Cao, X.; Zhang, L.; Zhou, G.; Li, J.; Xia, A.; Li, Y. Synergetic Integration of $Cu_{1.94}S$−$Zn_xCd_{1-x}S$ Heteronanorods for Enhanced Visible-Light-Driven Photocatalytic Hydrogen Production. *J. Am. Chem. Soc.* **2016**, *138*, 4286−4289.
(123) Fenton, J. L.; Steimle, B. C.; Schaak, R. E. Exploiting Crystallographic Regioselectivity To Engineer Asymmetric Three-Component Colloidal Nanoparticle Isomers Using Partial Cation Exchange Reactions. *J. Am. Chem. Soc.* **2018**, *140*, 6771−6775.
(124) Butterfield, A. G.; Steimle, B. C.; Schaak, R. E. Retrosynthetic Design of Morphologically Complex Metal Sulfide Nanoparticles Using Sequential Partial Cation Exchange and Chemical Etching. *ACS Mater. Lett.* **2020**, *2*, 1106−1114.
(125) Garcia-Herrera, L. F.; McAllister, H. P.; Xiong, H.; Wang, H.; Lord, R. W.; O'Boyle, S. K.; Imamovic, A.; Steimle, B. C.; Schaak, R. E.; Plass, K. E. Multistep Regioselectivity and Non-Kirkendall Anion Exchange of Copper Chalcogenide Nanorods. *Chem. Mater.* **2021**, *33*, 3841−3850.
(126) Robinson, R. D.; Sadtler, B.; Demchenko, D. O.; Erdonmez, C. K.; Wang, L. W.; Alivisatos, A. P. Spontaneous Superlattice Formation in Nanorods Through Partial Cation Exchange. *Science* **2007**, *317*, 355−358.
(127) Fenton, J. L.; Steimle, B. C.; Schaak, R. E. Tunable Intraparticle Frameworks for Creating Complex Heterostructured Nanoparticle Libraries. *Science* **2018**, *360*, 513−517.
(128) Nelson, A.; Ha, D.-H.; Robinson, R. D. Selective Etching of Copper Sulfide Nanoparticles and Heterostructures through Sulfur Abstraction: Phase Transformations and Optical Properties. *Chem. Mater.* **2016**, *28*, 8530−8541.
(129) Saruyama, M.; So, Y.-G.; Kimoto, K.; Taguchi, S.; Kanemitsu, Y.; Teranishi, T. Spontaneous Formation of Wurzite-CdS/Zinc Blende-CdTe Heterodimers through a Partial Anion Exchange Reaction. *J. Am. Chem. Soc.* **2011**, *133*, 17598−17601.
(130) Wang, W.; Dahl, M.; Yin, Y. Hollow Nanocrystals through the Nanoscale Kirkendall Effect. *Chem. Mater.* **2013**, *25*, 1179−1189.
(131) Bai, X.; Purcell-Milton, F.; Gun'ko, Y. K. Near-Infrared-Emitting CIZSe/CIZS/ZnS Colloidal Heteronanonail Structures. *Nanoscale* **2020**, *12*, 15295−15303.
(132) Bai, X.; Purcell-Milton, F.; Kehoe, D. K.; Gun'ko, Y. K. Photoluminescent, "ice-cream cone" Like Cu−In−(Zn)−S/ZnS Nanoheterostructures. *Sci. Rep.* **2022**, *12*, 5787.
(133) Xia, C.; Winckelmans, N.; Prins, P. T.; Bals, S.; Gerritsen, H. C.; de Mello Donegá, C. Near-Infrared-Emitting $CuInS_2$/ZnS Dot-in-Rod Colloidal Heteronanorods by Seeded Growth. *J. Am. Chem. Soc.* **2018**, *140*, 5755−5763.
(134) Xia, C.; Pedrazo-Tardajos, A.; Wang, D.; Meeldijk, J. D.; Gerritsen, H. C.; Bals, S.; de Mello Donega, C. Seeded Growth Combined with Cation Exchange for the Synthesis of Anisotropic $Cu_{2-x}S$/ZnS, $Cu_{2-x}S$, and $CuInS_2$ Nanorods. *Chem. Mater.* **2021**, *33*, 102−116.
(135) Portniagin, A. S.; Ning, J.; Wang, S.; Li, Z.; Sergeev, A. A.; Kershaw, S. V.; Zhong, X.; Rogach, A. L. Monodisperse $CuInS_2$/CdS and $CuInZnS_2$/CdS Core−Shell Nanorods with a Strong Near-Infrared Emission. *Adv. Opt. Mater.* **2022**, *10*, 2102590.
(136) Li, X.; Jiang, Z.; Ge, F.; Tao, C.-L.; Gu, W.; Xu, D.; Chen, F.; Xie, Z.; Cheng, F.; Wu, X.-J. Generalized Colloidal Approach for Preparing Epitaxial 1D/2D Heterostructures. *Chem. Mater.* **2022**, *34*, 4577−4586.
(137) Fafarman, A. T.; Koh, W. K.; Diroll, B. T.; Kim, D. K.; Ko, D. K.; Oh, S. J.; Ye, X.; Doan-Nguyen, V.; Crump, M. R.; Reifsnyder, D. C.; Murray, C. B.; Kagan, C. R. Thiocyanate-Capped Nanocrystal Colloids: Vibrational Reporter of Surface Chemistry and Solution-Based Route to Enhanced Coupling in Nanocrystal Solids. *J. Am. Chem. Soc.* **2011**, *133*, 15753−15761.
(138) Hu, J.; Li, L. S.; Yang, W.; Manna, L.; Wang, L. W.; Alivisatos, A. P. Linearly Polarized Emission from Colloidal Semiconductor Quantum Rods. *Science* **2001**, *292*, 2060−2063.
(139) Nam, S.; Oh, N.; Zhai, Y.; Shim, M. High Efficiency and Optical Anisotropy in Double-Heterojunction Nanorod Light-Emitting Diodes. *ACS Nano* **2015**, *9*, 878−885.
(140) Fan, F.; et al. Continuous-Wave Lasing in Colloidal Quantum Dot Solids Enabled by Facet-Selective Epitaxy. *Nature* **2017**, *544*, 75−79.
(141) Milleville, C. C.; Chen, E. Y.; Lennon, K. R.; Cleveland, J. M.; Kumar, A.; Zhang, J.; Bork, J. A.; Tessier, A.; Lebeau, J. M.; Chase, D. B.; Zide, J. M.; Doty, M. F. Engineering Efficient Photon Upconversion in Semiconductor Heterostructures. *ACS Nano* **2019**, *13*, 489−497.
(142) Rivest, J. B.; Swisher, S. L.; Fong, L. K.; Zheng, H.; Alivisatos, A. P. Assembled Monolayer Nanorod Heterojunctions. *ACS Nano* **2011**, *5*, 3811−3816.
(143) Lee, S.; Flanagan, J. C.; Kang, J.; Kim, J.; Shim, M.; Park, B. Integration of CdSe/$CdSe_xTe_{1-x}$ Type-II Heterojunction Nanorods into Hierarchically Porous TiO_2 Electrode for Efficient Solar Energy Conversion. *Sci. Rep.* **2015**, *5*, 17472.

https://doi.org/10.1021/acs.chemrev.2c00410
Chem. Rev. XXXX, XXX, XXX−XXX

(144) Oh, N.; et al. Double-Heterojunction Nanorod Light-Responsive LEDs for Display Applications. *Science* **2017**, *355*, 616−619.
(145) Huang, F.; Xu, J.; Chen, D.; Wang, Y. Sandwich-like $Cu_{1.94}S$-ZnS-$Cu_{1.94}S$ Nanoheterostructure: Structure, Formation Mechanism and Localized Surface Plasmon Resonance Behavior. *Nanotechnology* **2012**, *23*, 425604.
(146) Zhai, Y.; Shim, M. Effects of Copper Precursor Reactivity on the Shape and Phase of Copper Sulfide Nanocrystals. *Chem. Mater.* **2017**, *29*, 2390−2397.
(147) Wu, K.; Zhu, H.; Liu, Z.; Rodríguez-Córdoba, W.; Lian, T. Ultrafast Charge Separation and Long-Lived Charge Separated State in Photocatalytic CdS-Pt Nanorod Heterostructures. *J. Am. Chem. Soc.* **2012**, *134*, 10337−10340.
(148) Wu, K.; Chen, J.; Mcbride, J. R.; Lian, T. Efficient Hot-Electron Transfer by a Plasmon-Induced Interfacial Charge-Transfer Transition. *Science* **2015**, *349*, 632−635.
(149) Wu, K.; Lian, T. Quantum Confined Colloidal Nanorod Heterostructures for Solar-To-Fuel Conversion. *Chem. Soc. Rev.* **2016**, *45*, 3781−3810.
(150) Chen, G.; Qiu, H.; Prasad, P. N.; Chen, X. Upconversion Nanoparticles: Design, Nanochemistry, and Applications in Theranostics. *Chem. Rev.* **2014**, *114*, 5161−5214.
(151) Zhou, J.; Liu, Q.; Feng, W.; Sun, Y.; Li, F. Upconversion Luminescent Materials: Advances and Applications. *Chem. Rev.* **2015**, *115*, 395−465.
(152) Fischer, S.; Favilla, E.; Tonelli, M.; Goldschmidt, J. C. Record Efficient Upconverter Solar Cell Devices with Optimized Bifacial Silicon Solar Cells and Monocrystalline BaY_2F_8:30% Er^{3+} Upconverter. *Sol. Energy Mater. Sol. Cells* **2015**, *136*, 127−134.
(153) Sellers, D. G.; Zhang, J.; Chen, E. Y.; Zhong, Y.; Doty, M. F.; Zide, J. M. Novel Nanostructures for Efficient Photon Upconversion and High-Efficiency Photovoltaics. *Sol. Energy Mater. Sol. Cells* **2016**, *155*, 446−453.
(154) Yokoyama, D.; Sakaguchi, A.; Suzuki, M.; Adachi, C. Horizontal Molecular Orientation in Vacuum-Deposited Organic Amorphous Films of Hole and Electron Transport Materials. *Appl. Phys. Lett.* **2008**, *93*, 173302.
(155) Mashford, B. S.; Stevenson, M.; Popovic, Z.; Hamilton, C.; Zhou, Z.; Breen, C.; Steckel, J.; Bulovic, V.; Bawendi, M.; Coe-Sullivan, S.; Kazlas, P. T. High-Efficiency Quantum-Dot Light-Emitting Devices with Enhanced Charge Injection. *Nat. Photonics* **2013**, *7*, 407−412.
(156) Dai, X.; Zhang, Z.; Jin, Y.; Niu, Y.; Cao, H.; Liang, X.; Chen, L.; Wang, J.; Peng, X. Solution-Processed, High-Performance Light-Emitting Diodes Based on Quantum Dots. *Nature* **2014**, *515*, 96−99.
(157) Kim, T.; Kim, K. H.; Kim, S.; Choi, S. M.; Jang, H.; Seo, H. K.; Lee, H.; Chung, D. Y.; Jang, E. Efficient and Stable Blue Quantum Dot Light-Emitting Diode. *Nature* **2020**, *586*, 385−389.
(158) Cho, S. Y.; Oh, N.; Nam, S.; Jiang, Y.; Shim, M. Enhanced Device Lifetime of Double-Heterojunction Nanorod Light-Emitting Diodes. *Nanoscale* **2017**, *9*, 6103−6110.
(159) Koley, S.; Cui, J.; Panfil, Y. E.; Banin, U. Coupled Colloidal Quantum Dot Molecules. *Acc. Chem. Res.* **2021**, *54*, 1178−1188.

https://doi.org/10.1021/acs.chemrev.2c00410
Chem. Rev. XXXX, XXX, XXX−XXX